UCRL 9119

UNIVERSITY OF
CALIFORNIA

Ernest O. Lawrence

Radiation Laboratory

THE ELASTIC SCATTERING OF NEGATIVE PIONS BY PROTONS AT 230, 290, 370, AND 427 MEV

BERKELEY, CALIFORNIA

DISCLAIMER

UCRL-9119
UC-34 Physics and Mathematics
TID-4500 (15th Ed)

UNIVERSITY OF CALIFORNIA
Lawrence Radiation Laboratory
Berkeley, California

Contract No. W-7405-eng-48

THE ELASTIC SCATTERING OF NEGATIVE PIONS BY PROTONS AT 230, 290, 370, AND 427 MEV

Lester K. Goodwin

(Thesis)

April 7, 1960

Printed in USA. Price $2.25. Available from the
Office of Technical Services
U. S. Department of Commerce
Washington 25, D.C.

THE ELASTIC SCATTERING OF NEGATIVE PIONS BY PROTONS AT 230, 290, 370, AND 427 MEV

Contents

THE ELASTIC SCATTERING OF NEGATIVE PIONS BY PROTONS AT 230, 290, 370, AND 427 MEV

Lester K. Goodwin
(Thesis)

Lawrence Radiation Laboratory
University of California
Berkeley, California

April 7, 1960

ABSTRACT

The elastic differential cross section for the scattering of negative pions by hydrogen was measured at laboratory pion kinetic energies of 230, 290, 370, and 427 Mev. The elastically scattered pions were detected by a counter telescope which discriminated against recoil protons and inelastic pions on the basis of their shorter ranges. Nine differential-cross-section points obtained at each energy were fitted by a least-squares program to a Legendre polynomial series. At the three higher energies, D waves are required to give a satisfactory fit to the data. The real part of the forward-scattering amplitudes calculated from this experiment are in agreement with the predictions of dispersion theory. The results of this experiment in conjunction with data from other pion-nucleon scattering experiments support charge independence at these higher energies.

I. INTRODUCTION

The scattering of pions by nucleons has hitherto been extensively investigated from very low energies up to 300 Mev. In this energy region, dominated by the well known (3/2, 3/2) resonance, the experimental information is quite consistent and in good agreement with theory.[1]

Above 300 Mev, the data on pion scattering are quite meager. There are a few good measurements with high resolution and good statistics up to 330 Mev.[2] Above this energy, most of the existing data are of a qualitative nature.[3]

In the experiment described here, the differential elastic-scattering cross section for negative pions on protons has been measured at laboratory energies of 230, 290, 370, and 427 Mev for the incident pion. Also, the differential cross sections for combinations of the inelastic differential cross sections listed below have been measured.

In addition to the elastic-scattering interaction,

$$\pi^- + p \rightarrow \pi^- + p\,, \tag{1}$$

other competing interactions for π^- incident on protons are the elastic charge exchange,

$$\pi^- + p \rightarrow \pi^0 + n, \tag{2}$$

and the inelastic interactions leading to final states with two pions,

$$\pi^- + p \rightarrow \pi^- + \pi^+ + n,$$

$$\pi^- + \pi^0 + p, \tag{3}$$

and

$$\pi^0 + \pi^0 + n,$$

with a threshold at 170 Mev. The inelastic cross sections with three final-state pions with a threshold at 345 Mev have small enough cross sections at the highest energy measured in this experiment (427 Mev) so that their effect was not considered.

From the experiments described here on elastic scattering, information about the magnitudes of the various angular-momentum states present in the pion-nucleon interaction as a function of energy is obtained. The rapid increase of one of these waves is consistent with the tentative interpretation that the second resonance in the pion-proton interaction, occurring at 600 Mev[4,5] is a $D_{3/2}$ resonance.[6]

Another phase of the theoretical implications of these experiments is obtained from the dispersion-theory approach, whereby the inclusion of D and higher waves in the scattering analysis can be checked with the predictions of these theories by using the values of f^2 (pion-nucleon coupling constant) and zero-energy scattering lengths, which have been found to give good agreement with lower-energy data.[7]

The combination of π^- - p elastic scattering data with the data at the same energy for charge exchange and π^+ - p elastic scattering can be used, as pointed out by Stanghellini,[8] to infer a quantitative limit on the accuracy to which the charge-independence hypothesis is valid at these higher energies.

The most complete interpretation of pion-nucleon experiments so far has been based on an analysis in terms of scattering amplitudes and phase shifts. This approach is, of course, desirable at the higher energies also, and may be carried out consistently when the higher-energy data become adequate. The main complication introduced at these energies, in addition to the larger number of phase shifts necessary, is that these become complex quantities because of the existence of the inelastic channels. For a satisfactory determination of the phase shifts, the differential and total inelastic reactions possible have to be known to an accuracy comparable to that of the elastic data. A tentative set of phase shifts up to 600 Mev has been proposed by

Walker based on the existing elastic and inelastic data.[6] The validity and accuracy of this set can be confirmed as discussed above when the missing and poorly known data approach the accurate state of the elastic data obtained in this and similar experiments.[9]

II. EXPERIMENTAL METHOD

A. Experimental Arrangement

1. Magnets and Collimators

A diagram of the experimental arrangement is shown in Fig. 1. Negative pions were produced by inserting a beryllium target into the internal proton beam of the Berkeley synchrocyclotron. The proton beam had an energy of 730 Mev, and the target was 2-in. thick in the direction of the beam. The pions were deflected out of the cyclotron by its magnetic field through a thin aluminum window in the vacuum tank. A two-section quadrupole magnet with an aperture of 8-in. focused the emerging beam of pions, which then passed through a rotatable iron collimator 8-ft. long.

The pion beam was momentum-analyzed by passing it through a horizontal magnet system. During the initial run at the two higher energies, one wedge magnet was used (as shown in Fig. 1) which bent the beam through 55 deg. The entrance and exit angles of the beam were chosen to meet the wedge-magnet double-focusing condition so that a maximum intensity of useful beam could be obtained.[10] Further fine focusing was obtained from a three-section quadrupole magnet with an 8-in. aperture. During the final run at the two lower energies, where obtaining sufficient beam intensity was less difficult, two magnets replaced the one wedge magnet because the latter was unavailable at the time. Together they bent the beam 60 deg. A three-section quadrupole magnet of 4-in. aperture replaced the larger one used initially. A photograph of part of the second experimental arrangement is shown in Fig. 2.

The current settings for the bending magnets needed to obtain the negative-pion beam energies desired were determined approximately by wire-orbit measurements. The quadrupole magnets were adjusted to maximize the beam intensity for each setting of the bending-magnet system. The two-section quadrupole magnet almost doubled the beam

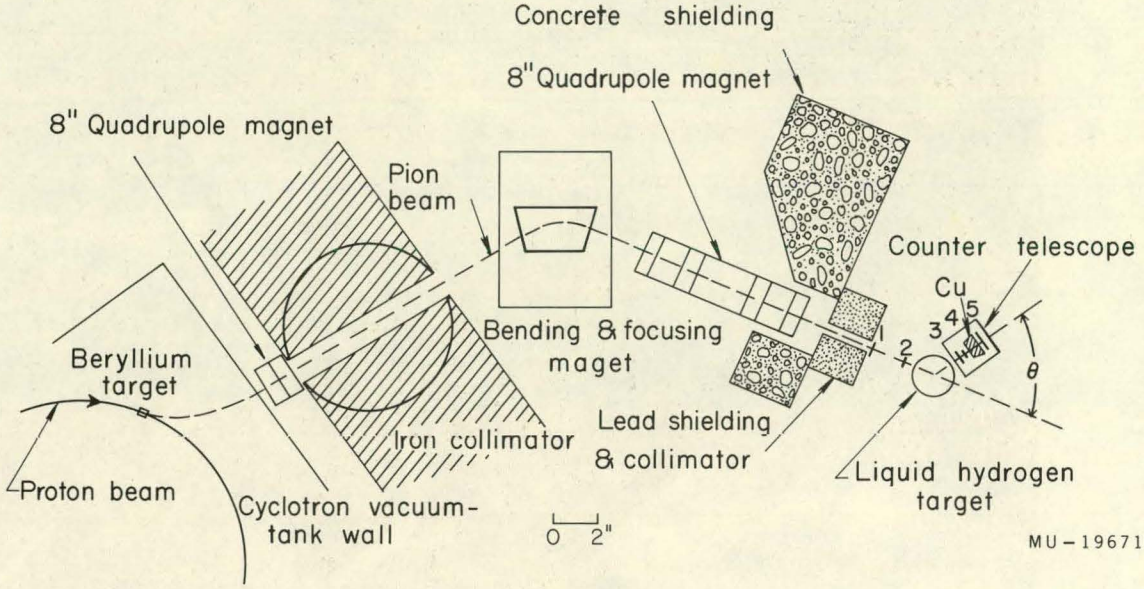

Fig. 1. Diagram of first-run experimental arrangement.

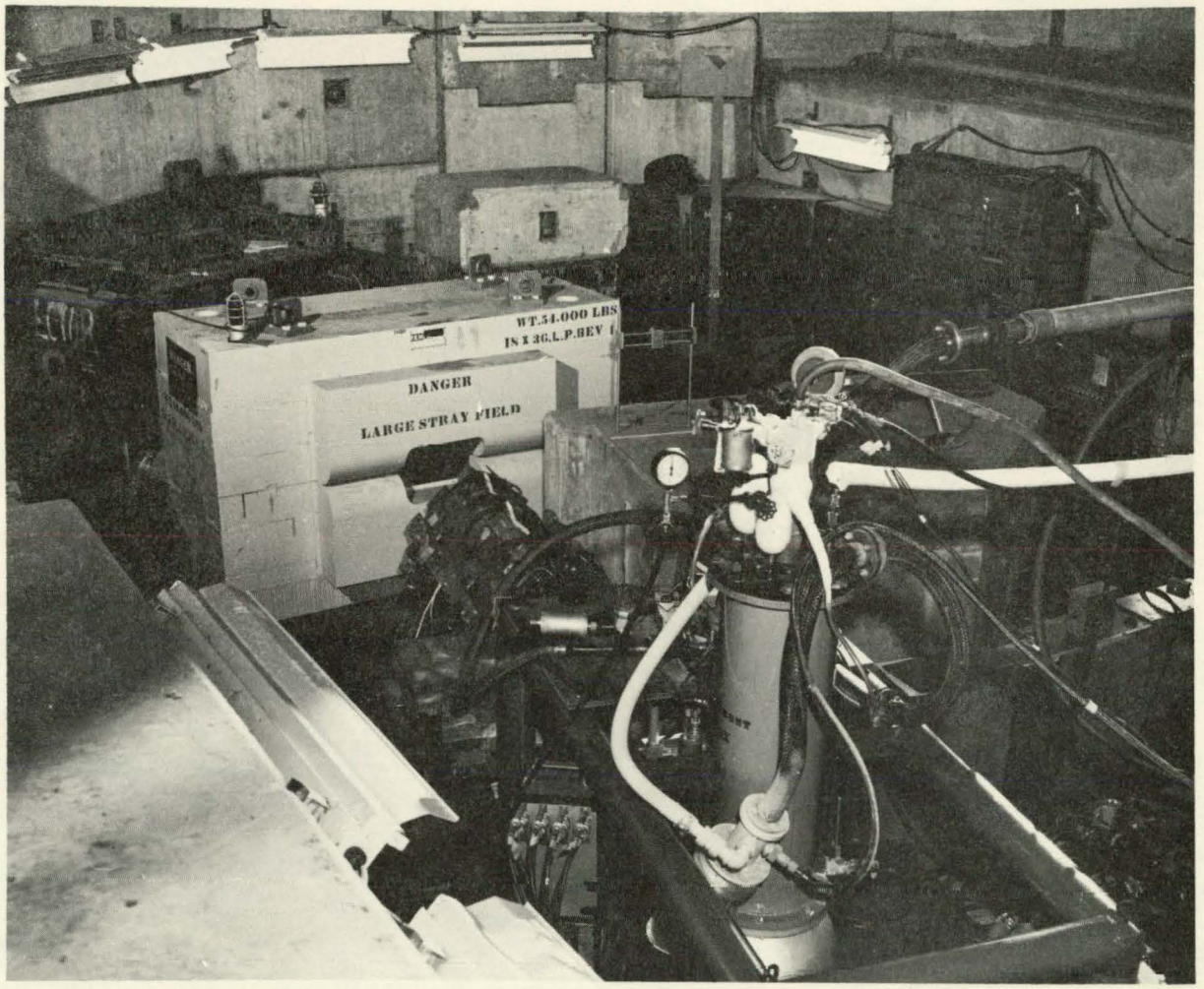

ZN-2395

Fig. 2. Part of second-run experimental arrangement.

intensity. The 4-in. aperture, three-section quadrupole gave an additional effect of similar magnitude. The 8-in aperture, three-section quadrupole following the double-focusing wedge magnet increased the intensity by only about 50%.

After the magnet system, the beam passed through a 2-ft. -thick lead collimating wall. Intensities in excess of 10^4 pions/sec were obtained for a 2-in. diam beam out of this collimator at all energies used.

2. Pion Beams

Four energies of pion beams were used. These beam energies with their energy spreads and contaminations are listed in Table I. The current settings of the bending magnets needed to give the desired energies were determined from wire-orbit data. Then the average energy and energy spread of the pion beam at each setting was accurately determined from range measurements in copper. From these range measurements, the fractional muon contaminations of the beams were also found. Sample differential and integral range curves for the 290-Mev pion beam are shown in Fig. 3. Three breaks are identified in the integral curve. Point A is the beginning of the pion ranges and point B their end. Point C is the end of the muon ranges, past which is found only an electron-shower tail. The method of measuring and interpreting these range curves is discussed in details in Appendix A.

Extrapolating the electron-shower tail of the range curves back to zero range using measured shower curves gives only an exaggerated upper limit to the electrons present in the beam.[11] The majority of electrons present in this tail come from charge-exchange reactions in the copper absorber. Consequently, the electron contamination of the beam was measured directly at the two lower energies by using a gas Čerenkov counter set to count particles with a β value greater than 0.99.[12] At the two higher energies, estimates were made of the upper limit to the number of electrons in the beam. Charge-exchange reactions in the lead wall followed by electron-pair formation from

Table I

Negative pion beam energies and contaminations

Pion beam energy, lab (Mev)	Use of beam	Muon contamination (%)	Electron contamination (%)
230 ± 6	Data run	15 ± 1	5 ± 1
290 ± 7	"	8 ± 1	1 ± 1
370 ± 9	"	4 ± 1	1 ± 1
427 ± 10	"	4 ± 2	1 ± 1
120 ± 7	Calibration	3 ± 3	---
155 ± 5	"	38 ± 3	---
192 ± 7	"	13 ± 2	---
294 ± 6	"	5 ± 1	---
378 ± 9	"	4 ± 1	---

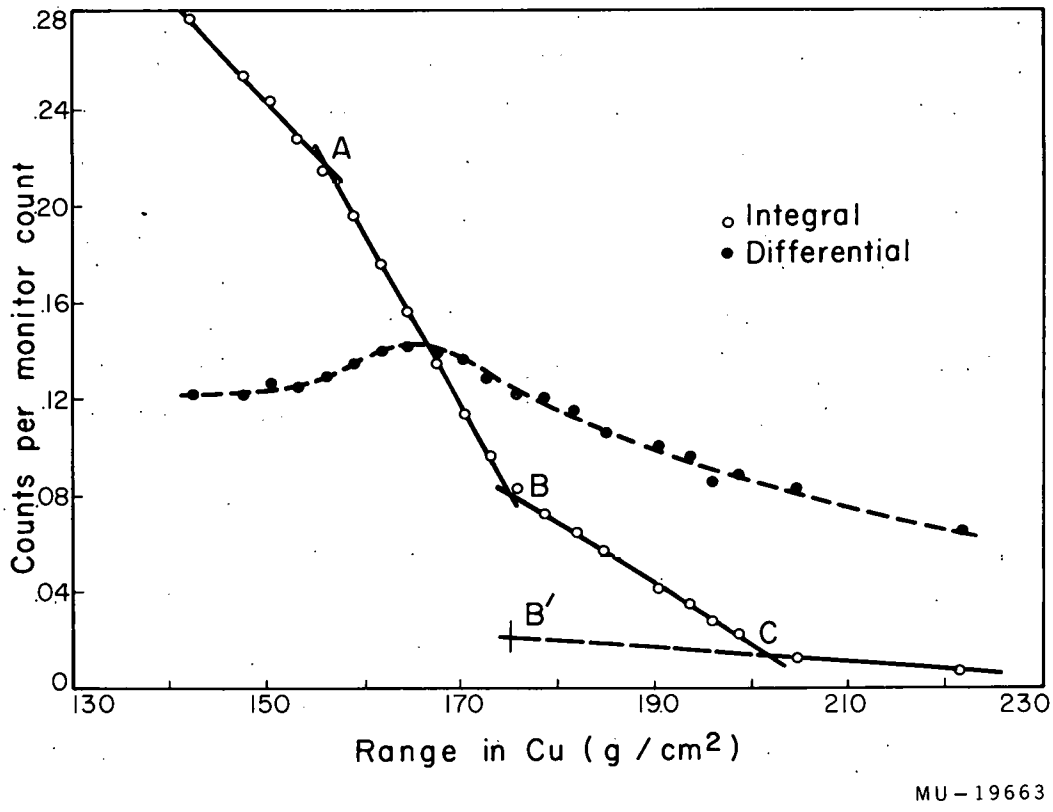

Fig. 3. Range curves in Cu for 290-Mev pion beam. (See text for explanation of points A, B, B', and C.)

the π^0 -decay gamma rays was shown by upper-limit calculations to contribute less than 0.5%. Electrons from the decay of π^0 mesons in the internal beryllium target were similarly estimated to give less than 1.5% . The electron contaminations obtained are given in Table I.

Horizontal and vertical beam profiles were measured in the position of the liquid hydrogen target with a 1/4-in. -square counter placed in coincidence with the two beam-monitor counters (No. 9, Table II). The profiles obtained at the two lower energies are shown in Fig. 4; similar ones were found at the two higher energies.

3. Counters

All the counters, with the exception of the gas Čerenkov counter, were plastic scintillation counters made of a solid solution of terphenyl in polystyrene. The sizes of the counters are listed in Table II. All the scintillators were viewed through lucite light pipes by RCA 6810A photomultiplier tubes.

During the data runs, counters 1 and 2 were used as monitors, and counters 3, 4, and 5 were combined into a counter telescope to detect elastically scattered pions. The location of these counters with respect to the hydrogen target is shown in Fig. 5. The details of the counter-telescope design are discussed in Section II. B. 1. The other counters listed in Table II were used in measuring the pion-beam properties discussed in Section II. A. 2.

4. Electronics

A block diagram of the electronics is shown in Fig. 6. The high monitor counting rate, up to 2×10^4 counts/sec, required high-speed electronic circuits. The synchrocyclotron operates at 64 pulses/sec, the pulse width being approximately 400 μsec. Each of these pulses had a fine structure of pulses about 1×10^{-8} sec wide spaced 5.4×10^{-8} sec apart due to the phase stability bunching of the accelerated protons. With existing electronics, it was not possible to resolve separate particles arriving in a single fine-structure pulse. The correction necessary because of multiple counts in one fine-structure pulse is discussed in Section II. C. 1. The counting rate during the coarse pulses reached 10^6 counts/sec.

Table II

Scintillation counter sizes

Counter No.	Width (in.)	Height (in.)	Diameter (in.)	Thickness (in.)
1	3.00	3.00		0.25
2			2.00	0.25
3	3.00	4.00		0.50
4	6.00	6.00		0.50
5	11.00	12.00		0.50
6			6.00	0.50
7			12.00	1.00
8			1.00	0.25
9	0.25	0.25		0.25

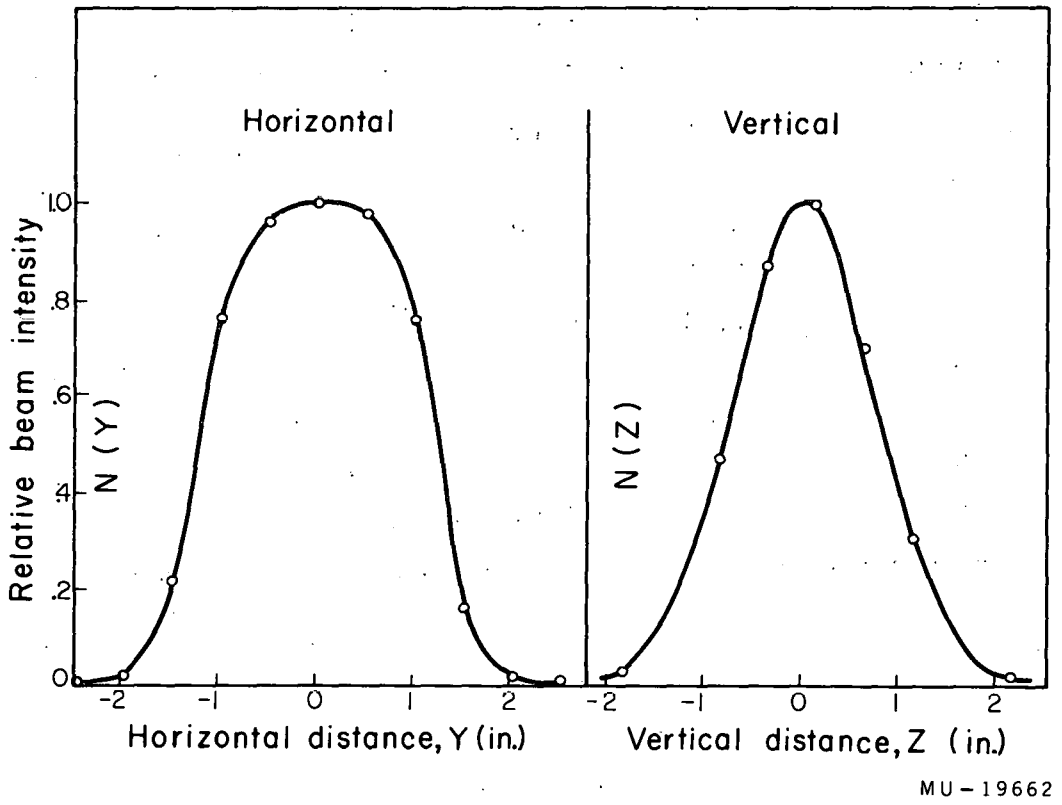

Fig. 4. Horizontal and vertical beam profiles taken with a 1/4-in. -square counter at the position of the liquid hydrogen target.

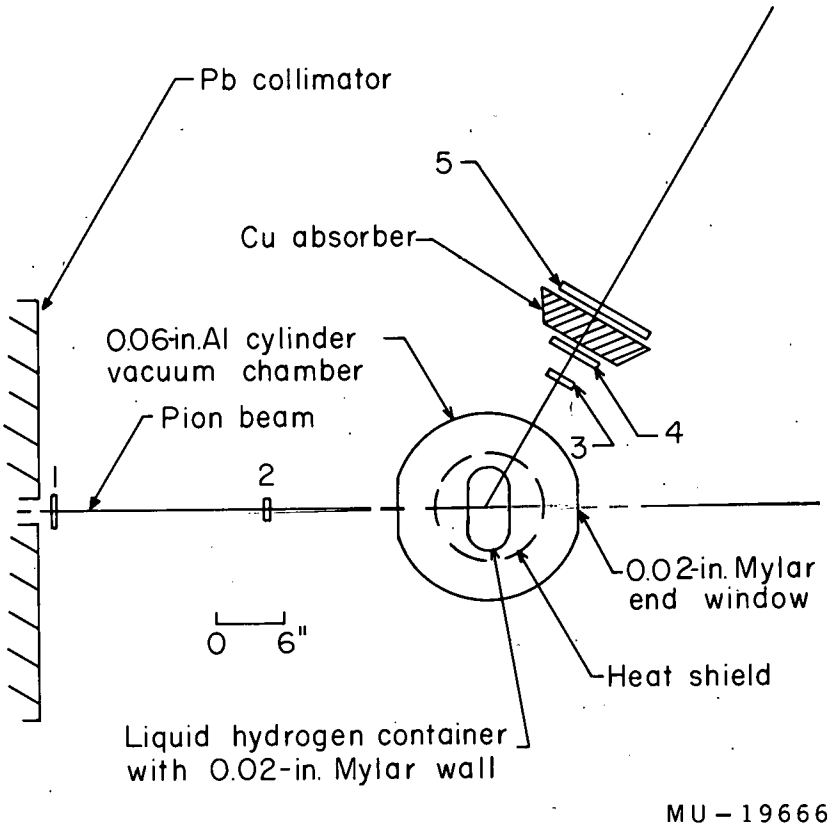

Fig. 5. Diagram showing the details of the hydrogen target and counter arrangement.

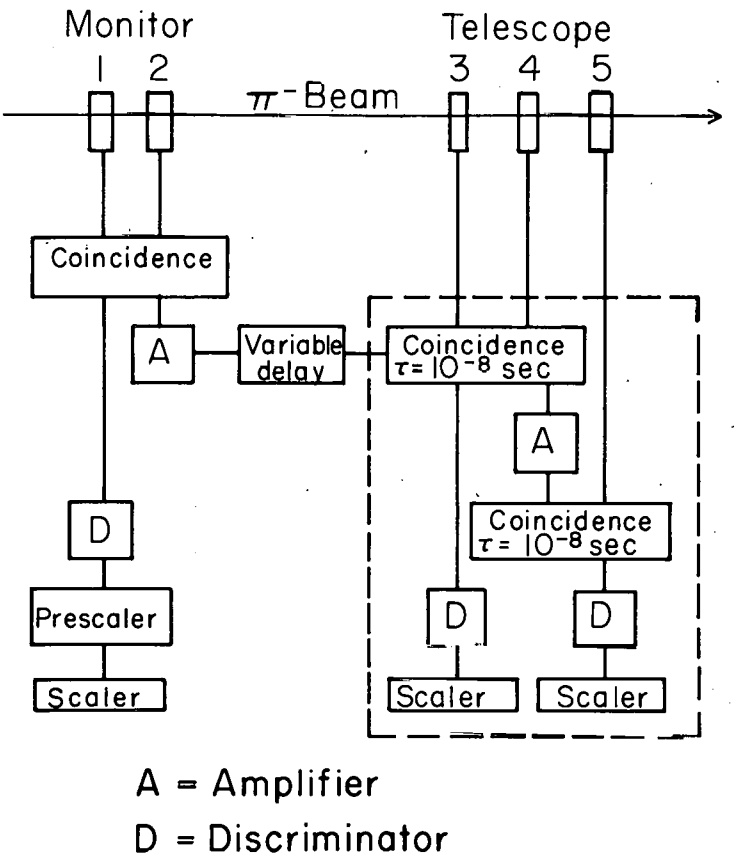

Fig. 6. Block diagram of electronics for monitor and counter telescope.

The Evans coincidence circuits[13] and Hewlett-Packard prescalers used were tested with a pulser and found to be able to operate continuously at 10 megacycles, enough to adequately resolve counts from the separate fine-structure pulses. Hewlett-Packard 460A distributed amplifiers were used for amplification of the pulses. Discriminators were used to select and uniformly shape all pulses above a selected threshold voltage.[14] To maintain constant-height output pulses from the 6810A photomultiplier tubes, large capacitors were used in the tube bases (1 μf in the last stage), which prevented voltage drops of more than 1%.

Both fourfold coincidences, 1234, and fivefold coincidences, 12345, were recorded in addition to the monitor doubles, 12. During measurements at forward angles, a 1/4-in.-thick counter with a 2-in.-diam semicular hole at one edge was used to define the incident beam more accurately. It was placed just before the target, and connected in anticoincidence with counters 1 and 2 to reduce direct beam spray into the telescope.

In order to obtain the data necessary to correct for multiple counts in one fine-structure pulse, 5.4×10^{-8} sec delay was inserted part of the time between the monitor and telescope. The interpretation of this data is discussed in Section II.C.1. To increase the speed of collecting data during the second run, the circuit area of Fig. 6. enclosed in a dotted rectangle was duplicated, and placed in parallel with the area shown. The signal from the monitor to this added circuit was delayed 5.4×10^{-8} sec, and data taken simultaneously. This added circuit was balanced occasionally by removing the delay and adjusting the discriminator setting as required to give equal numbers of counts from both circuits.

Before use, all counters were placed directly in the negative pion beam and the voltages on the photomultiplier tubes set at a value in the region where a plateau in the counting rate as a function of voltage occurred. Each counter in the final arrangement was tested for proper relative delay by varying its relative delay, and setting this delay at the

value where a maximum counting rate was found. Discriminator levels were set by replacing the counters with a pulser adjusted to give pulses at the output of each coincidence circuit about half of their saturation height.

Small Ru^{106}-Rh^{106} beta sources were attached to scintillators 3, 4, and 5. The strength of these sources was chosen to give single counts about ten times noise background in each counter. Daily measurements of the singles counting rate for each counter were made to check for constancy of amplification. Adjustments of the photomultiplier-tube voltages were made occasionally to keep this counting rate constant.

5. Target

The liquid hydrogen target used consisted of a small container with vertical side walls 5-in. high made of 0.02-in.-thick Mylar. Copper end pieces 4-in. wide and 8-in. long with 2-in.-radius ends supported the Mylar walls, which were bonded to the end plates with a Versamidepoxy mixture. The container was surrounded by a vacuum.

The small target chamber was attached to a large liquid hydrogen reservoir, which was jacketed in turn by the liquid nitrogen reservoir. The target was suspended directly in the π^- beam. The target could be emptied into or filled from the reservoir by closing or opening the target vent line.

Bulging of the mylar walls in the vacuum due to the 1-atmos pressure in the target was found by measurement to increase the effective thickness of the target 7% at liquid hydrogen temperature. The method of measuring the target thickness is discussed in Section III. A. 3. Mylar windows in the vacuum-chamber wall not only provided a low-Z material through which the beam passed but also allowed a visual check on the liquid hydrogen level in the target.

B. Counter Telescope

1. Design

Scintillation counters 3, 4, and 5 were grouped together into a rigid counter telescope with the relative positions shown in Figure 5. This telescope was placed on a dolly which pivoted about the center of the hydrogen target in a horizontal plane. The distance from this pivot axis to the telescope was variable so that the solid angle subtended could be adjusted. The height was also adjustable for initial alignment.

In order to distinguish the elastically scattered pions [interaction (1)] from their recoil protons and the other charged particles produced [interactions (3)], copper absorbers were placed between counters 3 and 5 in the telescope. Because the elastically scattered pions have greater range than any of the other charged particles at a given laboratory angle, the absorber thickness was chosen to allow only the elastic pions to reach counter 5.

Relativisitic two-body kinematic equations were used to find the maximum energy of pions from interactions (3) by taking as the mass of one of the outgoing particles the sum of a pion and nucleon mass. The relativisitic equations employed and sample results obtained are given in Appendix B. An IBM-650 computer program was used to make these calculations.

From the solutions to the relativisitic kinematics problem, it was found that the minimum amount of copper absorber needed in the counter telescope was approximately the same for a given kinetic energy of elastically scattered pions independent of the energy of the incident pion. In particular, it was found that the amount of copper needed in g/cm^2, C'_i, was less than that given by the simple linear equation

$$C_i = (T - 100)/2 \qquad (4)$$

where C_i is the ideal amount of absorber and T is the laboratory kinetic energy of the elastically scattered pions in Mev. This can be seen from Fig. 7, where C_i calculated from Eq. (4) and the actual minimum amount of absorber needed at the four energies used are plotted versus T. Consequently, the amount of absorber given by Eq. (4) was used throughout the experiment. In practice, the actual amount used, C, was the nearest amount greater than C_i that it was possible to get from combinations of existing pieces.

The size of counter 3 was chosen to have a reasonable solid angle of acceptance when placed as near the target as possible. The position of counter 5 was determined by the maximum thickness of copper (7 in.) needed at the highest energy. Then the sizes of counters 4 and 5 were chosen large enough to reduce losses from multiple coulomb scattering in the absorbers to less than 0.5%.

2. Calibration

For the highest energy scattered pions, the amount of copper required in the telescope transmitted only about 1/3 of the pions. Consequently, it was of great importance to measure accurately the efficiency of the counter telescope throughout its range of use.

The calibration of the counter telescope was carried out with essentially the same beam set up shown in Fig. 1. At the lower energies, minor adjustments of the wedge magnet and rotating collimator positions were necessary. The telescope was placed directly in the main pion beam just after the monitor counters. The number of telescope counts per monitor count gave the fraction of particles transmitted, F, after a small correction for accidentals was made.

The π^- beam energy was varied from 100 to 430 Mev by adjusting the current through the bending magnet. Settings of the current were obtained from wire-orbit data taken before the calibration run. Accurate determinations of the energy were made at five points by measuring ranges in copper (see Appendix A). The wire-orbit curves were used as extrapolation guides between these points to determine intermediate energies accurately.

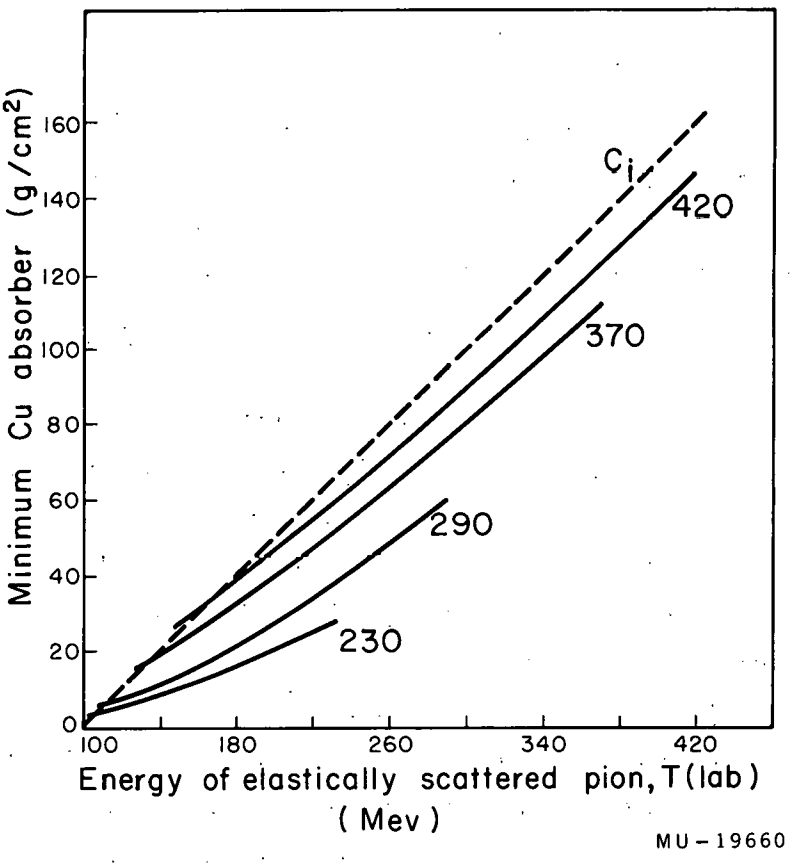

Fig. 7. Actual Cu absorber needed in counter telescope (solid line) at various beam energies and ideal amount, C_i, (dashed line) as a function of the kinetic energy of the elastically scattered pion.

At each energy at which the efficiency was measured, the nearest amount of copper obtainable to the amount given by Eq. (4) was used. In addition, 1/2-in. more and then 1/2-in. less was used. The telescope was also rotated horizontally at a few energies to measure the decrease in the efficiency resulting from the increased effective thickness of the copper. This latter effect was found to agree within experimental errors with what one would expect from geometrical considerations.

Because of the relatively higher fractional contamination in the pion beam at lower energies, it was necessary to determine carefully this contamination in order to minimize the effect of calibration errors on the final results. For this reason, a detailed discussion of the method of determining the muon contamination from range measurements is given in Appendix A.

The results of the calibration-range-curve measurements are given in Table I. The unusually high muon contamination at 155 Mev resulted from the physical impossibility of adjusting the position of the internal beryllium target properly at this energy. In Fig. 8 is shown a plot of the fractional muon contamination as a function of beam energy. A smooth curve connects the points from which contaminations at intermediate energies were read.

On the assumption that the muons count with 100% efficiency, the counter efficiency, E, is related to the measured fraction transmitted, F, and the fractional beam contamination, K, by the equation

$$E = (F - K) / (1 - K). \qquad (5)$$

In order to interpolate the measured efficiencies to energies and absorber thicknesses actually used, the efficiency values obtained from Eq. (5) above were fitted by the least squares method and the fitted function used in the extrapolation. The logarithm of the efficiency was fitted to a sum of two power series of the form

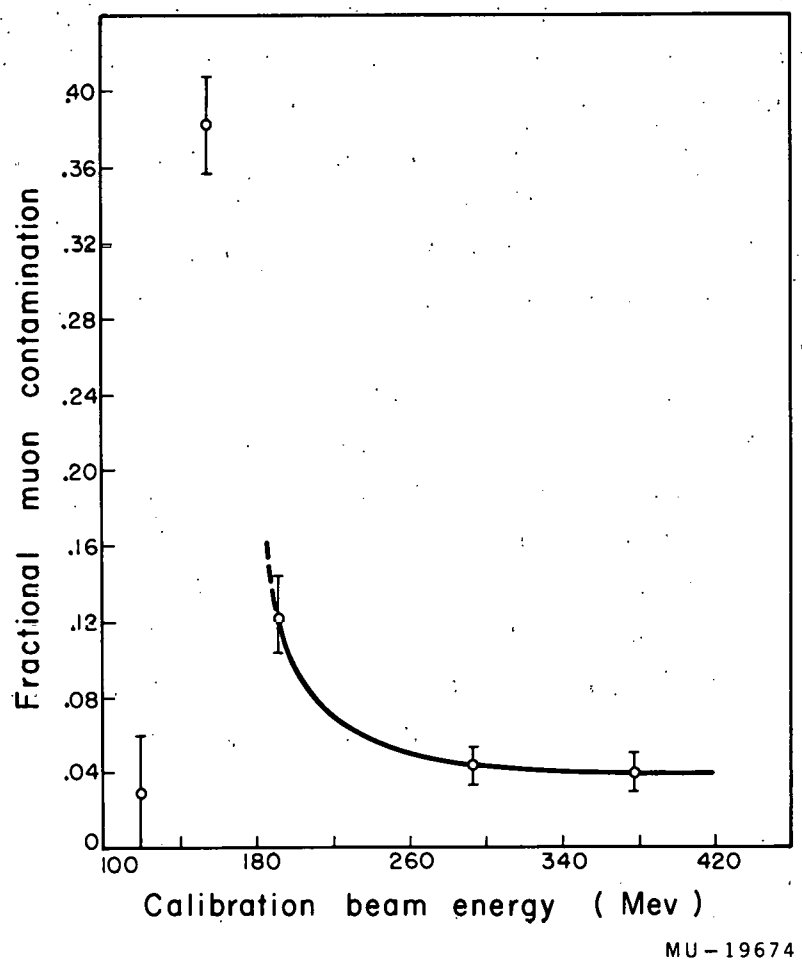

Fig. 8. Muon contamination in the calibration beam.

$$-\ln E = \sum_{j=0}^{N'} A_j (T - 100)^j + (C - C_i) \sum_{k=0}^{N''} B_k (T - 100)^k , \qquad (6)$$

where T is the energy of the elastically scattered pions in Mev, C is the actual copper thickness used in g/cm^2, and C_i is the ideal copper thickness in g/cm^2 obtained from Eq. (4).

To find the coefficients A_j and B_k in Eq. (6), first the measured values of $-\ln E$ at one beam energy and different absorber thicknesses, C, were fitted to a straight line. Then from this fit, the quantity $-\ln E$ was extrapolated to its value for $C = C_i$. The first summation in Eq. (6) must have this extrapolated value at that energy. Furthermore, the second summation in Eq. (6) must equal the slope of the linear fit at that energy. The values of N' and N'' necessary for these two summations to adequately fit their points at various energies were determined on the basis of a χ^2 test. The resulting values of A_j and B_k are listed in Table III. A plot of the ideal efficiency, E_i, (for $C = C_i$) is shown in Fig. 9. The least-squares fits were made by using an IBM-650 computer program. The least-squares formulas used are discussed in Appendix C.

Table III

Telescope efficiency constants

j, k	A_j	B_k
0	-1.235×10^{-1}	-8.204×10^{-8}
1	$+7.513\times10^{-3}$	$+1.046\times10^{-4}$
2	$+3.193\times10^{-7}$	$+2.207\times10^{-6}$
3	-3.837×10^{-8}	-2.917×10^{-8}
4	-2.331×10^{-9}	$+7.294\times10^{-11}$
5	$+2.131\times10^{-11}$	$+3.180\times10^{-13}$
6	-6.678×10^{-14}	-1.718×10^{-15}
7	$+7.189\times10^{-17}$	$+2.100\times10^{-18}$

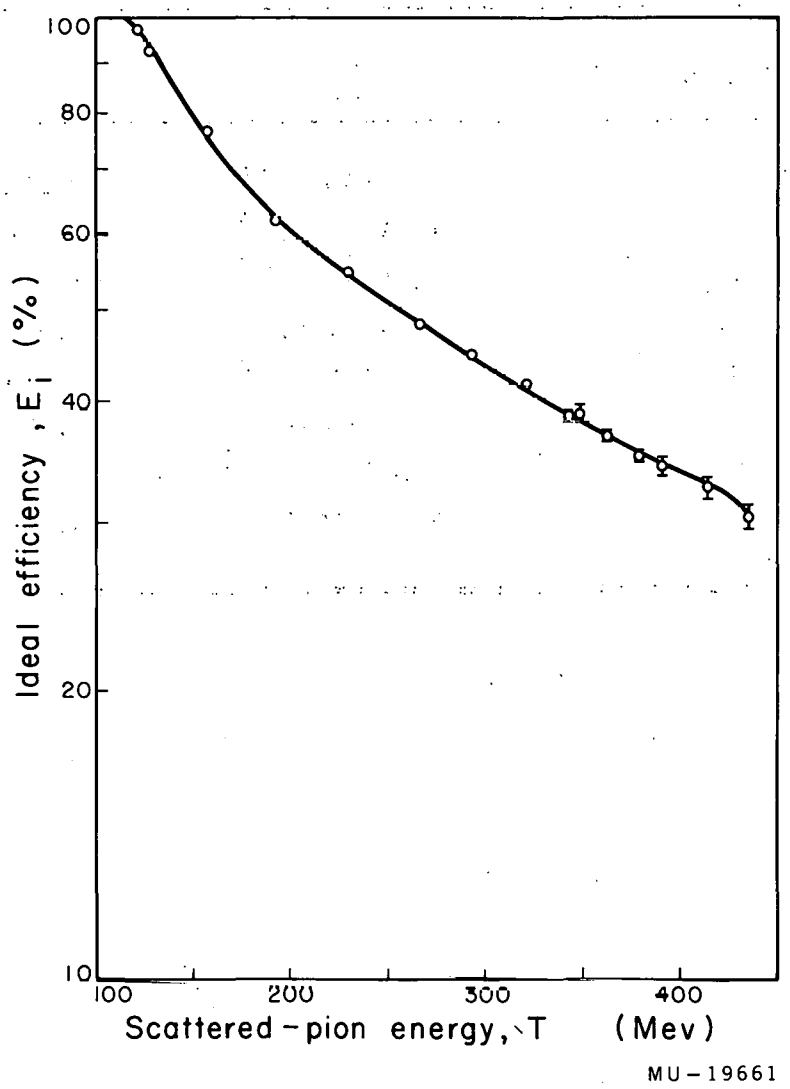

Fig. 9. Counter-telescope efficiency for the ideal amount of Cu absorber as a function of the elastically scattered pion energy.

C. Experimental Procedure

1. Accidentals and Background

The only important source of false counts in this experiment results from more than one particle passing through the monitor during a single fine-structure pulse. For reasons discussed in Section II. A. 4, it was not possible to resolve individual particles in one fine-structure pulse. The resulting number of extra counts in the telescope was measured by delaying the signal from the telescope relative to the monitor so that it arrived during a separate fine-structure pulse (Section II. A. 4). In order to minimize the error introduced by these accidentals, it was necessary to limit the pion-beam intensity throughout the runs to about 10^4 counts/second.

Other possible sources of accidentals were measured by similarily delaying pulses from individual counters relative to the rest. All of these other sources of accidentals proved to be negligible.

The background counts during the run were measured by cycling with the target empty and full at each different laboratory angle. This was done for both regular and accidental runs.

2. Counting Rates

The counting rate for scattered pions was of the order of 10 counts/min. In order to maximize the efficiency of taking data, the relative time spent measuring each of the four types of data outlined above was chosen equal to the square root of the telescope time counting rate for that type of data.

During the short cycles of measuring the four types of data, all conditions were kept as constant as possible. Laboratory angles were changed as a rule after each cycle.

D. Related Measurements

1. Simultaneous Experiments

While this experiment was being carried out on one side of the hydrogen target, other experiments were performed on the other side.

During the data run at 230 and 290 Mev, a measurement was made of the charge-exchange process given in interaction (2).[9] During the data run at 370 and 427 Mev, the positive-pion production processes given in interactions (3) were measured.[15]

In order to avoid a possible change in background level, data cycles were completed during periods when no changes in these other experiments were made.

2. Total Cross Section

Also in conjunction with this experiment, the total cross section was measured. This was done by using the same pion beam arrangement and magnet setting that were used in the differential-cross-section measurements. The small hydrogen target was replaced with one 4-ft long[16] and counter 7 was used as a detector. This experiment and its results are described elsewhere.[17] The importance to this experiment lies in the fact that the beam energies for which total cross sections were obtained were identical with those for which the elastic-scattering cross section was measured, independent of the uncertainties in determining these energies.

III. RESULTS

A. Differential Cross Section

1. Scattered Pions Counted

The number of real elastically scattered pions counted at each energy and angle was determined as follows. The quintuple coincidences, 12345, were analyzed for each cycle by first dividing by the corresponding number of monitor counts, 12. For the target-full and-empty runs separately, the real counting rate per monitor count, R, was determined by subtracting the accidental rate, A, from the total rate, T, using the formula

$$R = T - (M_T/M_A)\, A, \tag{7}$$

where M_T is the average monitor rate per unit time during a cycle for totals, and M_A is the average monitor rate per unit time during a cycle for accidentals. The ratio of monitor rates corrected the accidental rate when the accidentals were measured separately from the totals. When the simultaneous accidental circuit was included (see Sec. II. A. 4.), this ratio became one.

The background real counting rate, R_E, obtained by using Eq. (7) for the target-empty data, along with the corresponding target full rate, R_F, gave the final ratio of scattered particles per monitor count, I, counted by the telescope as

$$I = R_F - R_E \tag{8}$$

The values of I obtained from different cycles at a given energy and angle were combined by means of a weighted average to give the average number of scattered particles per monitor count, I_A, by

$$I_A = \sum_i I_i (\Delta I_i)^{-2} / \sum_i (\Delta I_i)^{-2}, \tag{9}$$

where ΔI is the standard deviation determined from counting statistics (see Sec. III. C. 1).

The average number of quintuple counts per monitor count, I_A, obtained at each energy and angle are listed in Table IV.

2. Efficiency

In order to correct for the number of elastic pions lost in the telescope absorber, it was necessary to divide the counts obtained at each point by the efficiency of the counter. This correction is included in Eq. (10).

The efficiency for the quintuple data was obtained from Eq. (6). The laboratory kinetic energy of the scattered pions needed, T, was found from the relativistic kinematics program (Appendix B). This energy was substituted in Eq. (4) to find the ideal absorber thickness, C_i. These two quantities with the actual absorber thickness, C, then were substituted into Eq. (6) to find the efficiency, E.

3. Target Constnat

The laboratory differential cross section, $d\sigma/d\Omega$, is related to the average scattered counts per monitor count, I_A, by the equation

$$d\sigma/d\Omega = I_A / E\Omega K . \qquad (10)$$

Where E is the efficiency, Ω is the solid angle subtended by the counter telescope, and K, the target constant, is the number of scattering centers per unit area normal to the beam direction. For hydrogen, it is given by the equation

$$K = N_0 \rho_H L \qquad (11)$$

where N_0 is Avogadro's number, ρ_H is the density of the liquid hydrogen in the target, and L is the average thickness of the target parallel to the beam direction.

Table IV

π^- elastic-scattering differential cross sections

Beam energy (Mev)	Lab. angle, θ (deg.)	Dist., D (in.)	Cu Absorb. thickness, C (g/cm^2)	$I_A \pm \Delta I_A$ ($\times 10^6$)	$d\sigma/d\Omega_T \pm \Delta d\sigma/d\Omega_T$ (mb/sterad)	$d\sigma/d\Omega^* \pm \Delta d\sigma/d\Omega^*$ (mb/sterad)	C.M. angle, θ^* (deg.)
230	15.0	30.00	65.69	14.75 ± 1.36	4.70 ± 0.43	3.03 ± 0.30	20.1
	22.4	23.00	62.85	24.90 ± 1.24	4.58 ± 0.23	3.14 ± 0.17	30.0
	38.0	23.00	54.40	16.01 ± 0.73	2.76 ± 0.13	2.11 ± 0.11	50.0
	54.6	15.00	45.82	24.00 ± 0.85	1.64 ± 0.06	1.45 ± 0.06	70.0
	72.7	15.00	42.97	13.18 ± 0.47	0.84 ± 0.03	0.89 ± 0.04	90.0
	92.7	15.00	19.94	16.18 ± 0.64	0.80 ± 0.03	1.06 ± 0.05	110.0
	114.8	15.00	8.67	20.98 ± 0.78	0.90 ± 0.03	1.48 ± 0.07	130.0
	139.5	15.00	2.98	28.02 ± 0.84	1.06 ± 0.03	2.11 ± 0.07	150.0
	159.4	23.00	2.98	12.29 ± 0.49	1.03 ± 0.04	2.23 ± 0.10	165.0
290	15.0	30.00	91.62	8.28 ± 1.71	2.99 ± 0.62	1.67 ± 0.33	20.8
	21.8	23.00	88.67	15.97 ± 1.02	3.35 ± 0.21	1.99 ± 0.12	30.0
	36.9	23.00	80.26	10.58 ± 0.66	2.15 ± 0.13	1.43 ± 0.08	50.0
	53.2	15.00	65.69	18.65 ± 0.97	1.49 ± 0.08	1.16 ± 0.06	70.0
	70.9	15.00	48.70	11.67 ± 0.58	0.80 ± 0.04	0.77 ± 0.04	90.0
	90.8	15.00	34.51	8.03 ± 0.39	0.48 ± 0.02	0.58 ± 0.02	110.0
	113.2	15.00	19.94	9.89 ± 0.45	0.50 ± 0.02	0.78 ± 0.03	130.0
	138.3	15.00	8.67	14.87 ± 0.75	0.65 ± 0.03	1.25 ± 0.05	150.0
	158.8	23.00	5.96	8.03 ± 0.45	0.77 ± 0.04	1.63 ± 0.08	165.0
370	10.4	48.00	134.40	2.23 ± 0.56	2.68 ± 0.67	1.14 ± 0.33	15.0
	20.9	23.00	126.03	10.27 ± 0.53	2.68 ± 0.14	1.38 ± 0.07	30.0
	35.5	15.00	114.65	20.08 ± 1.13	2.14 ± 0.12	1.26 ± 0.07	50.0
	51.3	15.00	94.62	16.02 ± 0.74	1.50 ± 0.07	1.06 ± 0.05	70.0
	68.7	15.00	74.28	9.20 ± 0.45	0.75 ± 0.04	0.67 ± 0.03	90.0
	88.4	15.00	54.40	5.56 ± 0.26	0.39 ± 0.02	0.45 ± 0.02	110.0
	111.0	15.00	34.23	6.83 ± 0.30	0.41 ± 0.02	0.63 ± 0.03	130.0
	136.7	15.00	22.92	7.49 ± 0.41	0.39 ± 0.02	0.74 ± 0.04	150.0
	157.9	23.00	19.44	3.56 ± 0.27	0.40 ± 0.03	0.87 ± 0.07	165.0
427	10.1	46.00	156.85	4.24 ± 0.66	4.97 ± 0.78	2.18 ± 0.37	15.0
	20.4	23.00	150.98	11.16 ± 1.47	3.20 ± 0.42	1.57 ± 0.21	30.0
	34.7	15.00	134.40	25.81 ± 1.60	2.95 ± 0.18	1.66 ± 0.11	50.1
	50.2	15.00	114.65	17.31 ± 0.89	1.80 ± 0.09	1.23 ± 0.07	70.2
	67.4	15.00	91.61	9.64 ± 0.52	0.87 ± 0.05	0.76 ± 0.04	90.2
	87.0	15.00	65.59	4.74 ± 0.27	0.35 ± 0.02	0.41 ± 0.03	110.2
	109.7	15.00	45.82	6.02 ± 0.33	0.41 ± 0.02	0.64 ± 0.04	130.2
	135.8	15.00	28.65	9.58 ± 0.47	0.54 ± 0.03	1.09 ± 0.06	150.1
	157.4	23.00	22.92	3.86 ± 0.24	0.47 ± 0.03	1.07 ± 0.07	165.1

The target pressure was about 1 atmos at all times. The density, ρ_H, used in Eq. (11) was actually taken as the difference between the densities of the target-full liquid and the target-empty vapor. These densities were obtained from the Cryogenic Data Book.[18] The liquid density used was that of boiling liquid hydrogen, 70.2 g/l. It was assumed that the target-empty vapor had a temperature between the boiling points of liquid hydrogen and liquid nitrogen. The vapor density was chosen as 0.9 ± 0.8 g/l, the average of the hydrogen gas densities at these two temperatures. The resultant value of ρ_H is 69.3 ± 0.8 g/l.

The average thickness of the target, L, was determined by measuring the bulging of the target sides at a matrix of points at room and liquid nitrogen temperature with 1 atmos more pressure inside the target than outside. These measurements were then linearly extrapolated to liquid hydrogen temperature. The resultant thicknesses were averaged with weights determined from the beam-profile measurements (Fig. 4) to get the average thickness, L, which was 4.230-in. The resultant value for the target constant, K, determined from Eq. (11) is $4.48 \pm 0.05 \times 10^{23}$ cm^{-2}.

B. Corrections

1. Finite Target and Telescope

The total cross section is determined from Eq. (10) strictly only for a point target and telescope. As a result, the values determined from this equation are in error because of the finite size of both the target and counter telescope.

To correct for this effect, the product of efficiency and solid angle, $E\Omega$, that appears in Eq. (10) must be replaced by an appropriate average value, $\overline{E\Omega}$. An average value for this product which gives by Eq. (10) a differential cross section equivalent to what a point target and telescope at the laboratory angle θ would measure was determined as follows. The target was divided into volume elements, V, and the counter into area elements, A, and the contributions from each element pair were summed by using the formula

$$\overline{E\Omega}(\theta) = \frac{\sum_V \sum_A N(V)\, E(V,A)\, F(\gamma)\, \Delta\Omega\,(V,A)}{F(\theta) \sum_V \sum_A N(V)} , \qquad (12)$$

where $N(V)$ is the relative beam intensity at the volume element, V, from the beam-profile measurements; $E(V,A)$ is the efficiency for the counter for pions scattered from volume element, V, into telescope area element, A; $F(\gamma)$ is the laboratory differential cross section at an angle, γ, obtained from the cross sections determined by using Eq. (10); γ is the angle the line between volume element, V, and area element, A, makes with the beam direction; and $\Delta\Omega(V,A)$ is the solid angle subtended at volume element, V, by the telescope area element, A.

More specific formulae for the quantities appearing in Eq. (12) are discussed in detail in Appendix D. These calculations were carried out using an IBM-650 computer program. This program divided the volume and area dimensions into n parts. The value of n beginning with 1 was increased by 1 and the two resultant values for $\overline{E\Omega}$ extrapolated to n equals infinity by the formula

$$\overline{E\Omega}_{\infty} = \frac{(n+1)^2 \overline{E\Omega}_{n+1} - n^2 \overline{E\Omega}_n}{(n+1)^2 - n^2} , \qquad (13)$$

which neglects terms of order $1/n^2$ and higher. The value of n was again increased until successive results from Eq. (13) agreed within 0.5%. This occurred with n equal to four in all instances. This correction for finite target and telescope size did not exceed 3% at any point.

The results obtained for the total scattered pion differential cross sections in the laboratory system, $d\sigma/d\Omega_T$, are listed in Table IV. These values were obtained from Eq. (10) after replacing $E\Omega$ by $\overline{E\Omega}$ from Eq. (12).

2. Beam Contamination and Attenuation

The muon and electron contamination of the incoming pion beam, the decay of pions into muons between the monitor and target, and the attenuation of both incident and scattered pions by the target material required that a negative correction be applied to the monitor counting rate, where the monitor is to be regarded as counting only those pions that enter into the scattering experiments. This correction does not change the form of the angular distribution, only its normalization.

The fractional beam contaminations were determined from range measurements (Appendix A), and the values obtained are listed in Table I.

3. Coulomb Scattering

The measured cross sections result from a combination of nuclear and coulomb scattering. At the energies and laboratory angles measured in this experiment, interference between these two types of scattering is negligible,[19,20] and the nuclear contribution can be determined by subtracting the coulomb cross sections from the measured cross sections. The laboratory coulomb cross sections $d\sigma/d\Omega_c$, in mb/sterad were obtained from the formula[21]

$$d\sigma/d\Omega_c = \frac{5.178}{(vp)^2 \sin^4(\theta/2)} , \qquad (14)$$

where p is the momentum of the pion in Mev/c for a pion of velocity, v, in units of c, the velocity of light.

4. Charge-Exchange Correction

The counter telescope acts as an approximately 1%-efficient counter of gamma rays. This results from pair production of electrons in the target, air, and front half of counter 3. Consequently, some decay gammas from the charge-exchange π^0 mesons are detected, and as a result, the measured cross sections must be reduced by 1% of the charge-exchange cross section at the same energy.

Only approximate values of these charge-exchange cross sections are needed because of the small size of this correction. Values from the literature were used for this purpose.[9] After the coulomb-corrected cross sections were converted to the center-of-mass system by using the values of $d\Omega/d\Omega^*$ obtained from the relativistic kinematics program (Appendix B), the contribution from the charge-exchange process was subtracted. The final barycentric differential cross section, $d\sigma/d\Omega^*$, obtained and the corresponding center-of-mass angle of scattering, θ^*, are listed in Table IV.

C. Errors

1. Counting Statistics

The statistical standard-deviation errors in the counting data were set equal to the square root of the corresponding number of counts. Monitor counts were taken as exact in this experiment, either because data was taken relative to them, or because the number of monitor counts was so large that the statistical error in them was negligible.

The errors in the quantities T and A appearing in Eq. (7) were arrived at, and they were propagated in the usual way through Eqs. (7) and (8) to give a standard deviation error, ΔI, on the quantity I of Eq. (8). The various values of I were averaged by using Eq. (9). Such averaging corresponds to making a least-squares polynomial fit of zero order. This calculation was done using an IBM-650 computer program (Appendix C), and the χ^2 test applied to test the consistency of the quantities, I_i, with the average. No improbable values of I were detected. Values of the standard deviation error, ΔI_A, obtained on the average quantities, I_A, are listed in Table IV.

2. Other Sources of Errors

The errors in the measured efficiency points, E, obtained from Eq. (5) arise effectively only from the uncertainty, ΔK, in the beam contamination, K, since the large number of counts taken makes the statistical error in the fraction transmitted, F, negligible. The error, ΔE, in the efficiency, E, is thus given by the equation

$$\Delta E = \frac{(1 - F)}{(1 - K)^2} \Delta K . \qquad (15)$$

This formula has been written down explicitly to show the important fact that the uncertainty in the efficiency is smaller than the uncertainty in the contamination fraction by a factor of about (1-F) for the small values of K observed. Thus the error in the measured efficiency is significantly less than the error in the beam contamination (1/10 as large for efficiencies greater than 90% for example). As a

result, even the uncertainty in the electron contamination of the calibration beam, which was estimated and included as a random error addition to ΔK, did not give efficiency errors in excess of 4% at any point. At most points, they were less than 2%. Error matrices were computed for both of the least-squares polynomial fits in Eq. (6), and the errors in the extrapolated efficiency values found from them.

The uncertainty given in the target constant, K, of Eq. (10) arose primarily from the uncertainty in the temperature of the hydrogen gas in the target when it was not full of liquid hydrogen (Sec. III. A. 3).

The error in the solid-angle determination was negligible. Small errors arising from the coulomb and charge-exchange correction were included.

Both the muon and electron contaminations were evaluated for the pion beams used in the data runs (Table I). The errors in these contaminations appear directly as errors in the correction factor multiplying the total angular distribution. Since they did not exceed 2%, however, they were included for convenience as additional random errors in the individual differential cross-section points because their contribution is small.

The combined results of all of these errors are listed as standard-deviation errors, $\Delta d\sigma/d\Omega^*$, on the final differential cross-section points, $d\sigma/d\Omega^*$, in Table IV. A plot of these differential cross sections is shown in Figure 10.

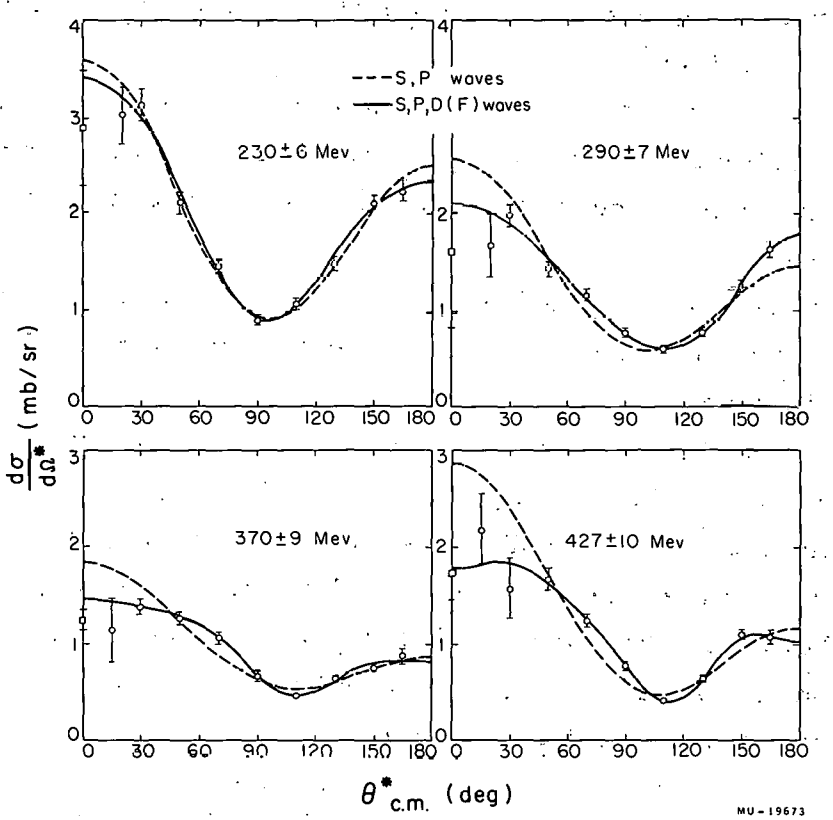

Fig. 10. Differential cross sections of elastically scattered pions for various incident beam energies. Dashed curve is least-squares fit with S and P waves only. Solid curve is best fit. The square points on the ordinates were obtained from dispersion relations and are not included in the fits.

D. Pion Production Cross Sections

Though this experiment was not primarily intended to measure cross sections for any of the pion-production processes given in interactions (3), some information about them is available from the quadruple, 1234 data taken. No copper absorber was placed between counters 3 and 4 at laboratory angles greater than 60 deg. Thus, all charged particles from reactions (1) and (3) are counted which have an energy above some threshold energy (approximately 25 Mev) necessary to penetrate through the target walls and counter 3 and 4. No recoil protons can appear at laboratory angles greater than 90 deg. Consequently, back of 90 deg in the laboratory system, and even at the smaller laboratory angles where recoil protons have energies below the detection threshold, only charged pions from interactions (1) and (3) are counted by counters 3 and 4.

Thus if at a laboratory angle, θ, the elastic differential cross section is $d\sigma/d\Omega_T$, and the differential cross section for the first of interactions (3) is $d\sigma_1/d\Omega$ and for the second it is $d\sigma_2/d\Omega$, then the measured quantity obtained from the quadrupole data, $d\sigma_4/d\Omega$, is given to a first approximation by the equation

$$d\sigma_4/d\Omega = d\sigma/d\Omega_T + f(2d\sigma_1/d\Omega + d\sigma_2/d\Omega), \qquad (16)$$

where f is the fraction of pions from interactions (3) that have an energy above the threshold energy for detection.

Since $d\sigma/d\Omega_T$ has been determined in this experiment (Table IV), and data concerning $d\sigma_1/d\Omega$ was obtained in another experiment (see Section II. D. 1),[15] information about $d\sigma_2/d\Omega$ is theoretically obtainable.

Consequently, the quadruples data, 1234, was analyzed in the same way as the quintuples data to get values from Eq. 9 for $I_A' \pm \Delta I_A'$ for the quadruples data (see Sec. III. A. 1). These values

are listed in Table V. These quantities in turn were used to find $d\sigma_4/d\Omega \pm \Delta d\sigma_4/d\Omega$ from Eq. 10 in the same way as $d\sigma/d\Omega_T \pm \Delta d\sigma/d\Omega_T$ was obtained for the quadruples data, except that the efficiency was assumed to be 100% since there was no absorber between counter 3 and 4. The results are listed in Table V for meaninfgul angles. From the results listed in Table IV, values for the quantity, $f(2d\sigma_1/d\Omega + d\sigma_2/d\Omega)$, were then calculated by means of Eq. (16). These values are listed in Table V.

It is necessary to evaluate the fraction, $f(\theta)$, appearing in Eq. (16). Because of the large statistical errors in all of these data, for simplicity the laboratory energy spectrum at all angles was assumed to have the approximate form, $\sin(2\pi T/T_{max})$, where T, the kinetic energy of the pion at that angle, has a maximum value, T_{max}. Thus, the fraction detected, $f(\theta)$, is given by the formula

$$f(\theta) = \left[\cos(2\pi T_{th} / T_{max}) + 1 \right]/2, \qquad (17)$$

where T_{th}, the energy threshold for detection, is taken as 25 ± 5 Mev. The values of f obtained from Eq. (17) are listed in Table V.

By using Eqs. (16) and (17), values for the quantity, $d(2\sigma_1 + \sigma_2)/d\Omega$, were obtained, and are listed in Table V. A plot of these points is shown in Fig. 11.

Table V

Pion-production differential-cross-section data

Beam energy (Mev)	Lab angle, θ (deg.)	Dist., D (in.)	$I_A' \pm \Delta I_A'$ ($\times 10^6$)	$d\sigma_4/d\Omega \pm \Delta d\sigma_4/d\Omega$ (mb/sterad)	$f\left[\frac{d(\sigma_1+\sigma_2)}{d\Omega} \pm \Delta\frac{d(2\sigma_1+\sigma_2)}{d\Omega}\right]$ (mb/Sterad)	$\sim f$ fraction	$\frac{d(2\sigma_1+\sigma_2)}{d\Omega} \pm \Delta\frac{d(2\sigma_1+\sigma_2)}{d\Omega}$ (mb/sterad)
230	72.7	15.00	22.63 ± 1.29	0.93 ± 0.05	0.09 ± .06	0.38 ± .17	0.24 ± .19
	92.7	15.00	22.06 ± 1.34	0.93 ± 0.06	0.13 ± .07	0.11 ± .15	1.18 ± 1.72
	114.8	15.00	23.38 ± 1.08	1.00 ± 0.05	0.10 ± .06	0	-
	139.5	15.00	24.85 ± 1.01	1.05 ± 0.04	0.01 ± .05	0	-
	159.4	23.00	11.99 ± 0.92	1.18 ± 0.09	0.15 ± .10	0	-
290	70.9	15.00	23.53 ± 1.86	0.99 ± 0.08	0.19 ± .09	0.79 ± .08	0.24 ± .12
	90.8	15.00	15.95 ± 1.09	0.66 ± 0.05	0.18 ± .06	0.69 ± .12	0.26 ± .10
	113.2	15.00	13.32 ± 0.84	0.56 ± 0.04	0.06 ± .05	0.52 ± .15	0.12 ± .11
	138.3	15.00	18.75 ± 1.21	0.80 ± 0.05	0.15 ± .06	0.33 ± .18	0.45 ± .31
	158.8	23.00	8.48 ± 1.35	0.84 ± 0.14	0.07 ± .15	0.21 ± .17	0.33 ± .76
370	88.4	15.00	18.77 ± 0.70	0.77 ± 0.03	0.38 ± .04	0.87 ± .05	0.44 ± .06
	111.0	15.00	14.02 ± 0.66	0.60 ± 0.03	0.19 ± .04	0.80 ± .08	0.24 ± .06
	136.7	15.00	12.52 ± 0.73	0.53 ± 0.03	0.14 ± .04	0.72 ± .10	0.19 ± .06
	157.9	23.00	6.78 ± 0.97	0.67 ± 0.10	0.27 ± .11	0.63 ± .13	0.43 ± .20
427	87.0	15.00	22.11 ± 1.02	0.89 ± 0.04	0.54 ± .05	0.92 ± .03	0.59 ± .06
	109.7	15.00	18.87 ± 1.07	0.80 ± 0.05	0.39 ± .06	0.88 ± .05	0.44 ± .07
	135.8	15.00	19.01 ± 1.06	0.81 ± 0.05	0.27 ± .06	0.81 ± .07	0.33 ± .08
	157.4	23.00	6.67 ± 0.92	0.66 ± 0.09	0.19 ± .10	0.77 ± .09	0.25 ± .14

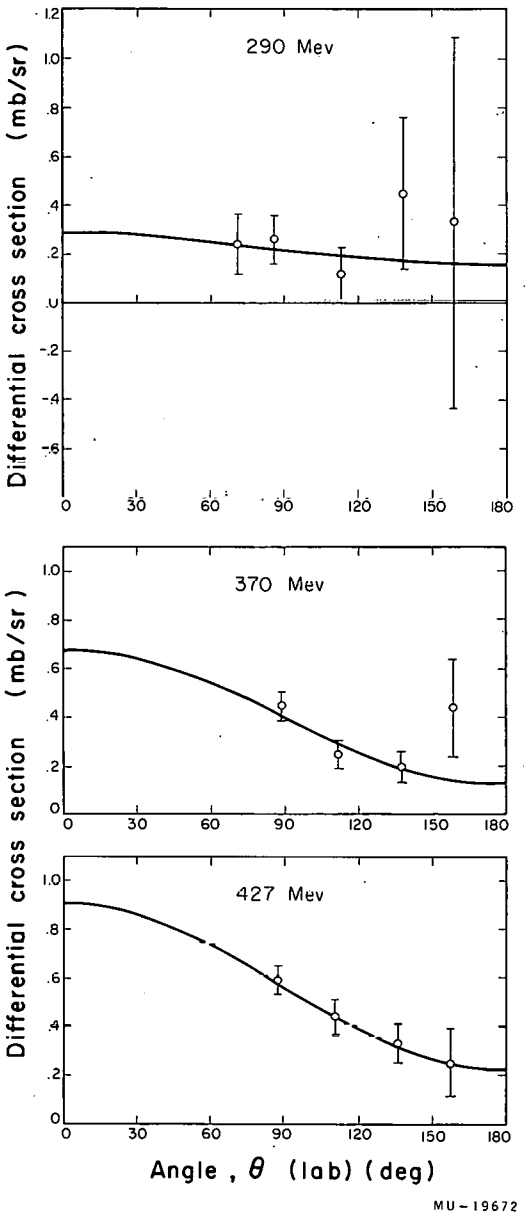

Fig. 11. Inelastic combined differential cross sections, $d(2\sigma_1 + \sigma_2)/d\Omega$ for various incident beam energies. Solid curves represent least-squares fits to a Legendre polynomial series.

IV. CONCLUSIONS

A. Partial Waves

To determine what orders of angular-momentum states are present in the elastic-scattering interaction, the measured differential cross sections, $d\sigma/d\Omega^*$ (Table IV) at each beam energy were least-squares fitted with a Legendre polynomial series of the form

$$\frac{d\sigma}{d\Omega^*}(\theta)^* = \sum_{\ell=0}^{n} A_\ell P_\ell (\cos\theta^*) . \qquad (18)$$

The magnitude of n necessary to fit adequately the data points at each energy was determined on the basis of a χ^2 test and supporting Fisher test (see Appendix C). The values of coefficients, A_ℓ, obtained for various values of n at each energy are listed in Table VI. Also listed in this table are the degrees of freedom, k; the values of χ^2 obtained; the probability, p, that χ^2 would exceed the value found in a random sample, and the Fisher probability, F, that A_n should be zero.

The first adequate and best fits determined on the basis of these statistical criteria are indicated by superscripts a and b in Table VI. For the best fits, the error matrices, C_{ij}, (See Appendix C) are given in Table VII. The theoretical curves obtained from Eq. (18) for S and P waves alone (n = 2) and for the best fits are shown in Fig. 10.

At 290 Mev and above, it can be seen that the probability that the data are consistent with fits based on S and P waves alone is less than 1%. In fact, the most probable values of n obtained include an F-wave interference term (n= 5) at 370 Mev and an F-wave term (n = 6) at 427 Mev. Thus the conclusion can be made that at 230 Mev only S and P waves are needed, but at the higher energies D waves are present and above 290 Mev F waves may be present, especially at 427 Mev.

Table VI

Results of least-squares legendre-polynomial fits to elastic π^- - p Data

Beam energy (Mev)	Order of fit n	Fitted coefficients A_0	A_1	A_2	A_3	A_4	A_5	A_6 (mb/sterad)	χ^2	K	p (%)	F (%)
230 ± 6	2[a]	1.65 ± 0.03	0.55 ± 0.06	1.40 ± 0.06					9.47	6	22	< 1
	3	1.66 ± 0.03	0.56 ± 0.06	1.42 ± 0.07	0.06 ± 0.07				8.85	5	16	60
	4[b]	1.66 ± 0.03	0.53 ± 0.06	1.38 ± 0.07	-0.01 ± 0.08	-0.15 ± 0.09			5.82	4	29	20
	5	1.66 ± 0.03	0.54 ± 0.06	1.38 ± 0.08	-0.01 ± 0.09	-0.14 ± 0.10	0.03 ± 0.10		5.71	3	18	85
	6	1.66 ± 0.03	0.53 ± 0.06	1.37 ± 0.09	-0.01 ± 0.10	-0.15 ± 0.11	0.01 ± 0.13	-0.06 ± 0.15	5.56	2	8	85
290 ± 7	2	1.10 ± 0.02	0.56 ± 0.04	0.91 ± 0.04					46.2	6	<1	< 1
	3[a]	1.09 ± 0.02	0.44 ± 0.05	0.70 ± 0.05	-0.34 ± 0.05				6.72	5	29	< 1
	4[b]	1.10 ± 0.02	0.45 ± 0.05	0.75 ± 0.06	-0.28 ± 0.07	0.11 ± 0.06			3.86	4	41	15
	5	1.10 ± 0.02	0.46 ± 0.05	0.76 ± 0.06	-0.24 ± 0.08	0.15 ± 0.08	0.06 ± 0.07		3.25	3	36	45
	6	1.10 ± 0.02	0.47 ± 0.05	0.77 ± 0.08	-0.23 ± 0.08	0.17 ± 0.09	0.08 ± 0.09	0.05 ± 0.12	3.08	2	25	50
370 ± 9	2	0.85 ± 0.02	0.49 ± 0.03	0.48 ± 0.03					48.2	6	<1	<1
	3	0.86 ± 0.02	0.45 ± 0.03	0.37 ± 0.04	-0.24 ± 0.04				16.8	5	1	2
	4[a]	0.86 ± 0.02	0.45 ± 0.03	0.32 ± 0.04	-0.32 ± 0.05	-0.16 ± 0.05			7.43	4	12	7
	5[b]	0.86 ± 0.02	0.45 ± 0.03	0.33 ± 0.04	-0.26 ± 0.06	-0.10 ± 0.07	0.11 ± 0.06		3.97	3	29	15
	6	0.86 ± 0.02	0.47 ± 0.03	0.37 ± 0.05	-0.24 ± 0.06	-0.07 ± 0.07	0.16 ± 0.08	0.09 ± 0.10	3.00	2	25	60
427 ± 10	2	1.08 ± 0.03	0.82 ± 0.06	0.88 ± 0.05					50.3	6	<1	< 1
	3	1.03 ± 0.03	0.65 ± 0.07	0.50 ± 0.07	-0.36 ± 0.06				18.8	5	<1	2
	4	1.03 ± 0.03	0.61 ± 0.07	0.52 ± 0.08	-0.49 ± 0.09	-0.17 ± 0.07			13.6	4	1	25
	5[a]	1.04 ± 0.03	0.63 ± 0.07	0.58 ± 0.08	-0.36 ± 0.10	0.01 ± 0.10	0.24 ± 0.08		4.58	3	21	8
	6[b]	1.04 ± 0.03	0.62 ± 0.07	0.57 ± 0.09	-0.39 ± 0.10	-0.06 ± 0.11	0.15 ± 0.11	-0.12 ± 0.10	3.05	2	23	35

[a] First adequate fit.

[b] Best fit.

Table VII

Best-fit error matrices, C_{ij}

Beam energy (Mev)	i	j = 0	1	2	3	4	5	6
230	0	0.00086	0.00099	0.00107	0.00062	-0.00012		
	1		0.00388	0.00286	0.00190	0.00127		
	2			0.00556	0.00356	0.00250		
	3				0.00702	0.00339		
	4					0.00763		
290	0	0.00049	0.00072	0.00057	0.00009	0.00011		
	1		0.00218	0.00175	0.00135	0.00052		
	2			0.00386	0.00296	0.00187		
	3				0.00434	0.00237		
	4					0.00399		
370	0	0.00029	0.00033	0.00019	-0.00004	-0.00001	0.00012	
	1		0.00108	0.00060	0.00047	0.00020	0.00023	
	2			0.00186	0.00155	0.00123	0.00052	
	3				0.00358	0.00261	0.00195	
	4					0.00423	0.00219	
	5						0.00358	
427	0	0.00093	0.00161	0.00148	0.00077	0.00035	0.00029	0.00008
	1		0.00456	0.00421	0.00313	0.00175	0.00070	0.00051
	2			0.00723	0.00629	0.00430	0.00199	0.00050
	3				0.00981	0.00802	0.00520	0.00213
	4					0.01206	0.00882	0.00537
	5						0.01208	0.00741
	6							0.01001

The total elastic cross section, σ_E, obtained by integrating the best-fit differential-cross-section curve is given by the formula

$$\sigma_E = 4\pi A_0 , \tag{19}$$

where A_0 is the lowest-order Legendre coefficient. The total elastic cross sections obtained by using Eq. (19) are listed in Table VIII. The differential cross sections at zero degrees, $d\sigma/d\Omega^*(0)$, obtained from Eq. (18) by setting $\theta = 0$ and propagating errors using the error matrix (See Appendix C) are also listed in Table VIII.

Table VIII

Total elastic and forward differential cross section from best least-squares fits, and total cross sections

Beam energy (Mev)	$\sigma_E \pm \Delta\sigma_E$ (mb)	$\frac{d\sigma}{d\Omega^*}(0) \pm \Delta\frac{d\sigma}{d\Omega^*}(0)$ (mb/sterad)	$\sigma_T \pm \Delta\sigma_T$ (mb)
230	20.8 ± 0.4	3.40 ± 0.25	48 ± 2
290	13.8 ± 0.3	2.12 ± 0.20	31 ± 2
370	10.9 ± 0.2	1.41 ± 0.20	28.9 ± 1.4
427	13.0 ± 0.4	1.81 ± 0.43	29,5 ± 1.4

B. Dispersion Relations

Dispersion theory relates the differential forward-scattering cross section, $d\sigma/d\Omega^*(0)$, to the total cross section, σ_T, at the same energy by the dispersion relation

$$d\sigma/d\Omega^*(0) = f_r^2 + (p^*/4\pi)\sigma_T , \qquad (20)$$

where p^* is the momentum of the incident pion in the barycentric system (see Appendix B) and f_r is the real part of the forward-scattering amplitude for which values are predicted by the dispersion theory.[7] The units employed in Eq. (20) are those where $\hbar = c = M_\pi = 1$ (in these terms the cross-section unit is 20 mb, and the momentum unit is 140 Mev/c).

Equation (20) may be used to determine values for the real part of the forward scattering amplitude, f_r, from measured values of the forward differential cross section and the total cross section. Measured values of the forward differential cross section were taken from Table VIII, and total-cross-section values were obtained from the literature[2,5] and are also listed in Table VIII. The calculated values of f_r are given in Table IX, and are plotted in Fig. 12. At the two higher energies, the value of f_r^2 was found to be slightly negative but much smaller than its statistical error, so it was taken as zero. The error given on f_r was determined in this instance assuming f_r^2 to be equal to its error. Recent theoretical values[22] of f_r obtained by using the latest values of the π - p total cross sections at higher energies[5] in the dispersion integrals are also shown in Fig. 12 for comparison. Within statistics, no disagreement with these values, and to this extent no disagreement with dispersion theory, is found.

Equation (20) may be used alternatively to obtain the forward-scattering amplitude, $d\sigma/d\Omega^*(0)$, from the measured total cross sections, and theoretical values of the real part of the forward-scattering amplitude mentioned above. The points obtained by this

Table IX

Measured values of the real part of forward scattering amplitude

Beam energy (Mev)	f_r (fermis)
230	0.29 ± .10
290	0.28 ± .13
370	0.00 ± .12
427	0.00 ± .14

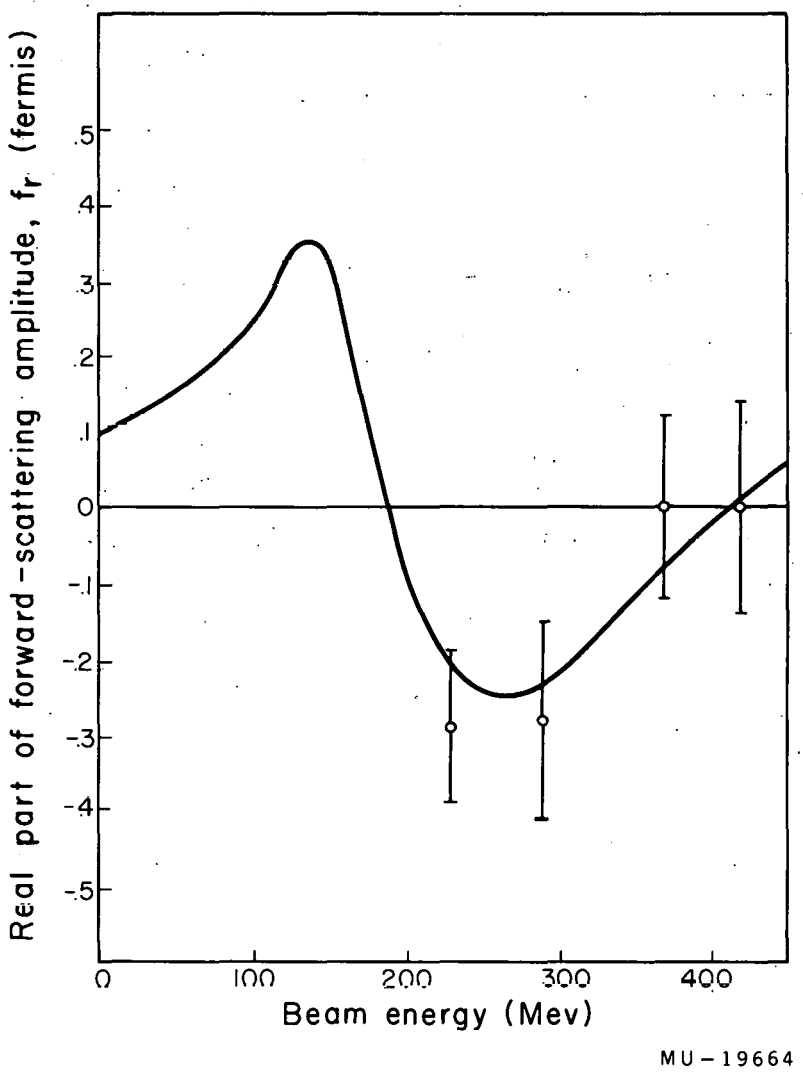

Fig. 12. The real part of the forward-scattering amplitude. Solid curve represents the theoretical values.

procedure are shown in Fig. 10. Because of the relatively small contribution to the differential cross section from the real part compared to the imaginary part at these energies, even a 100% error in the real part does not significantly effect the magnitude of the differential cross sections or its error. Thus the zero-degree differential cross sections shown in Fig. 10 depend effectively only upon the experimentally determined total cross sections, and to this extent these points may be considered as additional experimental points at zero degrees. When these points are included in the fit by using Eq. (18), little change in the coefficients results (see Ref. 25 for typical results).

C. Charge Independence

A test for charge independence given by Stanghellini[8] can be made by testing the validity of the equation

$$2f_{t0}^2 = (|f_{r+} - f_{r-}|)^2 + (f_{i+} - f_{i-})^2 , \qquad (21)$$

where 0, +, and - indicate respectively, π^- charge exchange, π^+ elastic scattering, and π^- elastic scattering by protons. For any one of these interactions, we can define the quantities appearing in Eq. (21) by

$$f_{tj}^2 = d\sigma / d\Omega^* (0) , \qquad (22)$$

which is the forward-differential-scattering amplitude (j = 0, +, -), and

$$f_{ij} = (p^*/4\pi)\sigma_i , \qquad (23)$$

where p^* is the barycentric pion momentum (see Appendix B) and σ_i is the total cross section for the particular interaction. The forward-scattering amplitude, f_r, is related to f_t and f_i by the equation

$$f_{rj}^2 = f_{tj}^2 - f_{ij}^2 . \qquad (24)$$

Letting a_L be the calculated value for the left side of Eq. (21), and a_R be the calculated value for the right side, a measure of the validity of Eq. (21) is given by

$$V = \Delta(a_L - a_R)\, a/_L , \qquad (25)$$

where Δ indicates the uncertainty in the quantity.

Using this method, Stanghellini has found no disagreement with charge independence up through 307 Mev within the accuracy obtainable using available data. Using the values for $\pi^+ - p$ scattering cross sections at 360 Mev[23] in conjunction with $\pi^- - p$ charge-exchange data at 371 Mev,[9] the following values were calculated for a_L and a_R from $\pi^- - p$ elastic data obtained in this experiment: $a_R = 0.26 \pm .30$ and $a_L = 0.39 \pm .02$. Using these results in Eq. (25) gives $V \approx 77\%$. This can be interpreted to mean that the equation is valid within 77%, which is more accurate than the greater than 100% error in a_R. Thus, no disagreement with charge independence is found at 370 Mev either. Sufficient data is not available at 427 Mev to make this test.

D. Phase Shifts

If we assume charge independence to be valid, the general formula for pion-nucleon scattering is[24]

$$d\sigma/d\Omega^{*} = \lambda^{2}\left\{\left|\sum_{\tau=1/2}^{3/2} C_{\tau} \sum_{\ell=0}^{L} \left[(\ell+1)\, a^{\ell,\tau}_{j=\ell+1/2} + \ell\, a^{\ell,\tau}_{j=\ell-1/2}\right] P^{0}_{\ell}(\cos\theta^{*})\right|^{2}\right.$$

$$\left. + \left|\sum_{\tau=1/2}^{3/2} C_{\tau} \sum_{\ell=1}^{L} \left(a^{\ell,\tau}_{j=\ell+1/2} - a^{\ell,\tau}_{j=\ell-1/2}\right) P^{1}_{\ell}(\cos\theta^{*})\right|^{2}\right\} \tag{26}$$

where the amplitude, a, is given in terms of its phase shift, α, by

$$a = \frac{e^{2i\alpha} - 1}{2i} = e^{i\alpha} \sin\alpha\,, \tag{27}$$

and where λ is the wave length of the pion ($\lambda = \hbar/p^{*}$), τ is the total isotopic spin, C_{τ} is an appropriate product of Clebsch-Gordon coefficients for the particular interaction considered, L is the maximum-order angular-momentum state that enters, and the P's are Legendre polynomials. The values of C_{τ} for various pion-nucelon interactions are given in Table X.

In Eq. (26) there are present $4L+2$ phase shifts. Elastic π^{-} - p data alone can be fitted with only $2L+1$ parameters (see Sec. IV. A). Consequently, π^{-} - p charge-exchange or π^{+} - p scattering data is also needed in order to determine all of the phase shifts. At the higher energies where pion inelastic processes enter, these phase shifts also have nonnegligible imaginary parts. Pion-production data must then be included to evaluate these imaginary components. More than one acceptable set of solutions may be found

Table X

Clebsch-Gordon Product Coefficients, C_π

Interaction	$C_{1/2}$	$C_{3/2}$
$\pi^- + p \rightarrow \pi^- + p$	2/3	1/3
$\pi^- + p \rightarrow \pi^0 + N$	$\sqrt{2/3}$	$\sqrt{2/3}$
$\pi^+ + p \rightarrow \pi^+ + p$	0	1

as a rule, and polarization data is then needed to resolve these ambiguities. Tracking is necessary, i.e. phase shifts must vary continuously from established values as energy increases, Before one can use available data for different interactions taken at slightly different energies, it must be properly extrapolated to corresponding energies. The paucity of accurate data, especially inelastic data,[15] currently available above 300 Mev leads to large uncertainties in the phase shifts obtainable.

However, this problem has been undertaken by Walker, et al[6] in the energy region from 300 to 600 Mev. The 370-427-Mev results of this experiment which have been reported already[25] have been used in conjunction with data taken by Crittenden et al.[3] and others to obtain one set of phase shifts tracked from lower-energy solutions. Of particular interest are the D-wave phase shifts, δ, obtained from 370 through 600 Mev, which are listed in Table XI.

The D-wave phase shifts consistent with the results of this experiment at 290 Mev may be approximately determined by using other available pion-scattering results at neighboring energies, and by assuming the D-wave phase shifts to be small at this energy.

The method for doing this depends upon least-squares fitting the elastic π^- - p differential cross sections to a power series in cos θ^* of the form

$$d\sigma/d\Omega^* = \sum_{\ell=0}^{n} A''_\ell \ (\cos\theta^*)^\ell \ . \qquad (28)$$

Least-squares fits of the form given in Eq. (28) were made to the data obtained in this experiment using the least-squares program (Appendix C); and the resulting values of A'' for the best fits obtained are listed in Table XII

If the assumption is now made that F waves and higher phase shifts are all zero, A''_4, the coefficient of the $(\cos\theta^*)^4$ term in Eq. (28), is a function of the D-wave phase shifts only. If it is further assumed that these D-wave phase shifts, σ, are small, then the D-wave

Table XI

Experimental D-wave shifts δ

Beam energy (Mev)	δ_{13} (deg)	δ_{33} (deg)	δ_{15} (deg)	δ_{35} (deg)
290	$-2.6^{+2.6}_{-1.6}$	2.2	-3.5	-3.5
370[a]	4.5^{+2}_{-0}	2.5	-1.6 ± 1	-3.0
430[a]	7.1^{+2}_{-1}	2.5	-1.6 ± 1	-3.0
460[a]	18.5 ± 2	$2.8 \pm .7$	$-0.5 \pm .1$	$-3.7 \pm .1$
600[a]	18.3^{+35}_{-0}	3.5^{+0}_{-3}	-5.6 ± 2	-3.3^{+2}_{-0}

[a]From Walker et al.[6]

Table XII

Results of least-squares Power-series best fits to elastic π^- - p data

Beam energy (Mev)	Order of fit (n)	Fitted coefficients A''_0	A''_1	A''_2	A''_3	A''_4	A''_5	A''_6
		(mb/sterad)						
230	4	0.91 ± 0.04	0.55 ± 0.14	2.63 ± 0.36	-0.02 ± 0.25	-0.66 ± 0.45		
290	4	0.76 ± 0.03	0.87 ± 0.09	0.72 ± 0.21	-0.69 ± 0.16	0.47 ± 0.27		
370	5	0.66 ± 0.03	1.03 ± 0.11	0.89 ± 0.25	-1.56 ± 0.51	-0.45 ± 0.32	0.81 ± 0.52	
427	6	0.77 ± 0.05	1.47 ± 0.21	0.20 ± 0.70	-2.19 ± 1.05	2.43 ± 0.20	1.10 ± 1.06	-1.99 ± 1.78

amplitudes, a_D, in Eq. (27) may be approximated by

$$a_D = \delta \tag{29}$$

By expanding the Legendre polynomials in Eq. (26) into sines and cosines, and collecting the coefficients of the resulting $(\cos\theta^*)^4$ term, formulae relating the δ's to the A''_4 coefficients may be found. Under the above assumptions there results, for π^- - p elastic scattering,

$$(2\delta_{13} + \delta_{33} + 3\delta_{15} + \tfrac{3}{2}\,\delta_{35})^2 - (-\delta_{13} - \tfrac{1}{2}\,\delta_{33} + \delta_{15} + \tfrac{1}{2}\,\delta_{35})^2 = A''_4/\lambda\!\!\!^{-2}$$

and, for π^- - p charge-exchange scattering, (30)

$$\tfrac{1}{2}(2\delta_{13} - 2\delta_{33} + 3\delta_{15} - 3\delta_{35})^2 - 2(-\delta_{13} + \delta_{33} + \delta_{15} - \delta_{35})^2 = A''_4/\lambda\!\!\!^{-2}. \tag{31}$$

By now employing some experimental results, the four D-wave phase shifts that appear in Eqs. (30) and (31) may be determined. First, the fact that no D waves were detected experimentally in π^- - p charge-exchange scattering through 371 Mev may be used to set A''_4 in Eq. (31) equal to zero. This leads either to the condition that

$$\delta_{15} = \delta_{35} \tag{32}$$

or to the condition that

$$\delta_{15} - \delta_{35} = 4(\delta_{33} - \delta_{13}) \tag{33}$$

The first condition, Eq. (32), is almost satisfied within statistics by all the phase shifts obtained by Walker et al. (Table XI), whereas the second condition, Eq. (33), is not. This fact helps to explain why no D waves were detected up through 371 Mev in the π^- - p charge-exchange results,[9] and indicates that little or no pure D-wave

contribution may be expected in the charge-exchange results up through 600 Mev, even though the D-wave phase shifts are not zero.

If it is now assumed that Eq. (32) is approximately correct, the unknowns in Eq. (30) may be reduced to three. By employing the two D-wave isotopic-spin-triplet phase shifts experimentally determined near 300 Mev by both Foote et al.[26] and Korenchendo and Zinov,[27] it becomes possible to calculate the two singlet δ's also. Following Walker, the values of δ_{33} and δ_{35} were taken as the average of these two experimental determinations, which immediately determines δ_{15} by Eq. (32). These three values were inserted into Eq. (30) and δ_{13} determined using $A_1'' = 0.47 \pm 0.27$ (Table XII), and $\lambda\!\!\!^{-} = 0.6764 \times 10^{-13}$ cm. Two solutions were found. The one around 25 deg was discarded because it violates the continuity condition. The phase shifts finally obtained are listed in Table XI. The statistical error quoted on δ_{13} results only from the uncertainty in the value of A_4'' used.

Theoretical values for the D-wave phase shifts have been predicted by Chew et al on the basis of dispersion theory.[24] The formulae given for these phase shifts in units where $\hbar = c = M_\pi = 1$ are

$$\delta_{13} = -\lambda_D \left[1 + \frac{11}{9}\left(\frac{w}{w+w_r}\right)^2\right],$$

$$\delta_{33} = \lambda_D \left[2 - \frac{28}{9}\left(\frac{w}{w+w_r}\right)^2\right], \qquad (34)$$

$$\delta_{15} = \lambda_D \left[4 - \frac{32}{9}\left(\frac{w}{w+w_r}\right)^2\right],$$

and

$$\delta_{35} = -\lambda_D \left[8 + \frac{8}{9}\left(\frac{w}{w+w_r}\right)^2\right],$$

where

$$\lambda_D = (1/15)\,(f^2/M)\,(p^*)^5/w^2 \qquad (35)$$

and

$$w = E^* - M. \qquad (36)$$

The value of f^2 has been taken as 0.08, M is the mass of the proton, and p^* and E^* are the barycentric momentum and total energy (Appendix B). The value of w at the 3/2 - 3/2 resonance, w_r, was taken as 2.1. The resulting theoretical values of the phase shifts at various beam energies are listed in Table XIII.

As can be seen by comparing the experimental phase shifts with their theoretical values, there is little agreement in magnitude, and the signs are reversed for δ_{13} and δ_{15}.

A further check was made by substituting the theoretical phase shifts at 290 Mev into Eq. (30) to obtain a value for A''_4 for the π^- - p elastic-scattering results. This gave $A''_4 = 0.14$, about one and one-half standard deviations low.

Good agreement was not anticipated by the authors of these theoretical phase shifts because the effects of possible pion-pion interactions were neglected. Recent results indicate the importance of such interactions at these energies,[15] and the disagreement found here can be attributed to them.

Table XIII

Theoretical D-wave phase shifts, δ

Beam energy (Mev)	δ_{13} (deg)	δ_{33} (deg)	δ_{15} (deg)	δ_{35} (deg)
290	-1.26	0.27	0.75	-2.15
370	-2.72	0.47	1.40	-4.23
430	-3.76	0.55	1.77	-5.53

E. Pion-Production Processes

The combined pion-production differential cross sections measured, $d(2\sigma_1 + \sigma_2)/d\Omega$, (see Sec. III. D.) are listed in Table V and shown in Fig. 11. Because of the complications introduced by the three-body pion-production kinematics, no attempt was made here to separate the two differential cross sections or convert them to the barycentric system by using previously measured values of $d\sigma_1/d\Omega^*$.[15] Rather, the combined laboratory differential cross sections were fitted with a Legendre polynomial series of the form

$$d(2\sigma_1 + \sigma_2)/d = A_o' \; P_o (\cos\theta) + A_1' \; P_1' (\cos\theta) , \tag{37}$$

which gave an excellent fit at all three energies as determined by a χ^2 test (Appendix C). The total cross section, $2\sigma_1 + \sigma_2$, was then obtained from Eq. (19), and the results are listed in Table XIV.

In Table XIV are also given the values of σ_1 previously reported.[15] By subtracting these values from $2\sigma_1 + \sigma_2$, the charged-inelastic-pion cross section, $\sigma_1 + \sigma_2$, was obtained, and the results are listed in Table XIV. These results are in statistical agreement with other published values.[3]

By again subtracting σ_1 from $\sigma_1 + \sigma_2$, values for σ_2 alone were obtained, and are listed in Table XIV. The errors on these values of σ_2, the total cross section for the second interaction of interactions (3), are so large that little can be learned quantitatively. However, qualitatively it appears that σ_2 may be decreasing with energy, and at the higher energies it certainly appears to be significantly smaller than σ_1, the total cross section for the first interaction of interactions (3).

Table XIV

Pion-production total cross section

Beam energy (Mev)	Total cross sections			
	$2\sigma_1 + \sigma_2$ (mb)	σ_1 (mb)	$\sigma_1 + \sigma_2$ (mb)	σ_2 (mb)
290	2.8 ± 0.8	0.4 ± 0.2	2.4 ± 0.8	2.0 ± 0.9
370	5.0 ± 0.7	1.93 ± 0.37	3.1 ± 0.8	1.2 ± 1.0
427	7.1 ± 0.7	3.36 ± 0.74	3.7 ± 1.0	0.4 ± 1.6

ACKNOWLEDGMENTS

I am indebted to Professor A. C. Helmholz for his guidance and encouragement throughout my graduate work. Thanks are especially due to Drs. Robert Kenney and Victor Perez-Mendez for their helpful advice and assistance during this experiment. Special mention is also due Drs. Walton Perkins, III and John Caris for their generous help throughout the experimental program. I should also like to thank the many other members of our group who contributed their time during the cyclotron runs.

Finally, I wish to thank Mr. James Vale and the cyclotron crew for their assistance and cooperation during the course of the experimental work.

This work was done under the auspices of the U. S. Atomic Energy Commission.

APPENDICES

A. The Measurement and Interpretation of Pion Ranges in Copper

The two purposes of determining the ranges of pion beams are:

(a) to determine the average energy and energy spread of the pions in the beam,

(b) to determine the fraction of muons in the pion beam.

The electronics setup used in measuring the ranges is shown schematically in Fig. 13. Counters 6 and 7 (Table II) were used as detectors for the integral and differential ranges, respectively. The electronics circuit is essentially the same as that used in the data collection runs and is discussed in Section II. A. 4. The end portions of typical integral and differential range curves is shown in Fig. 3.

In order to illustrate the form of the measured range curves, an idealized pion-beam energy distribution and the integral range curve that would result from it are shown in Fig. 14. In part A of this figure, the beam energy distribution has been broken down into three components. The first is the pion portion. The remaining two components constitute the muon portion. The first part consists of muons resulting from pion decays before the beam reaches the analyzing magnet, which therefore have the same momentum range as the pions. The second part consists of muons resulting from pion decays after the beam has passed the analyzing magnet, which thus have a wide momentum spread. In part B of Fig. 14, the idealized integral range curve that results is shown. The six breaks that should appear in this range curve have been numbered for reference.

Analysis of an actual integral range curve begins with identification of the breaks seen in it with the breaks expected in the idealized curve. Not all of the breaks expected can be identified, however, because many effects enter which modify the form of the observed curves. The energy distributions of the beam components are not actually rectangular, but rounded. Consequently, the observed breaks are less distinct. Also, there is present an electron-shower background which drops off approximately exponentially with absorber

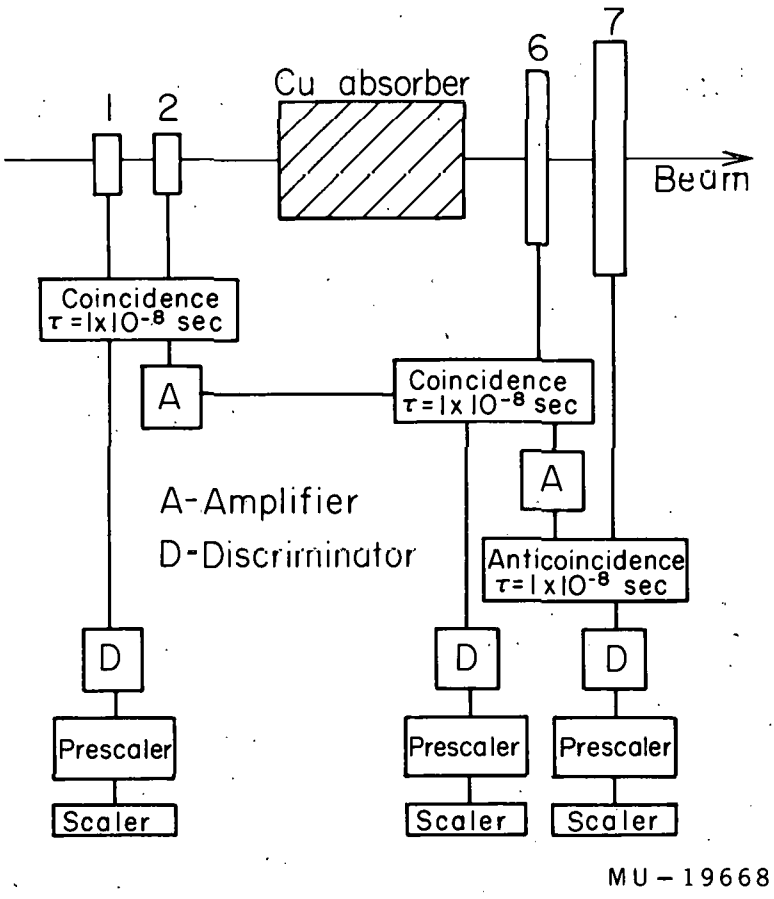

Fig. 13. Block diagram of the electronics used in the simultaneous integral and differential range-curve measurements in Cu.

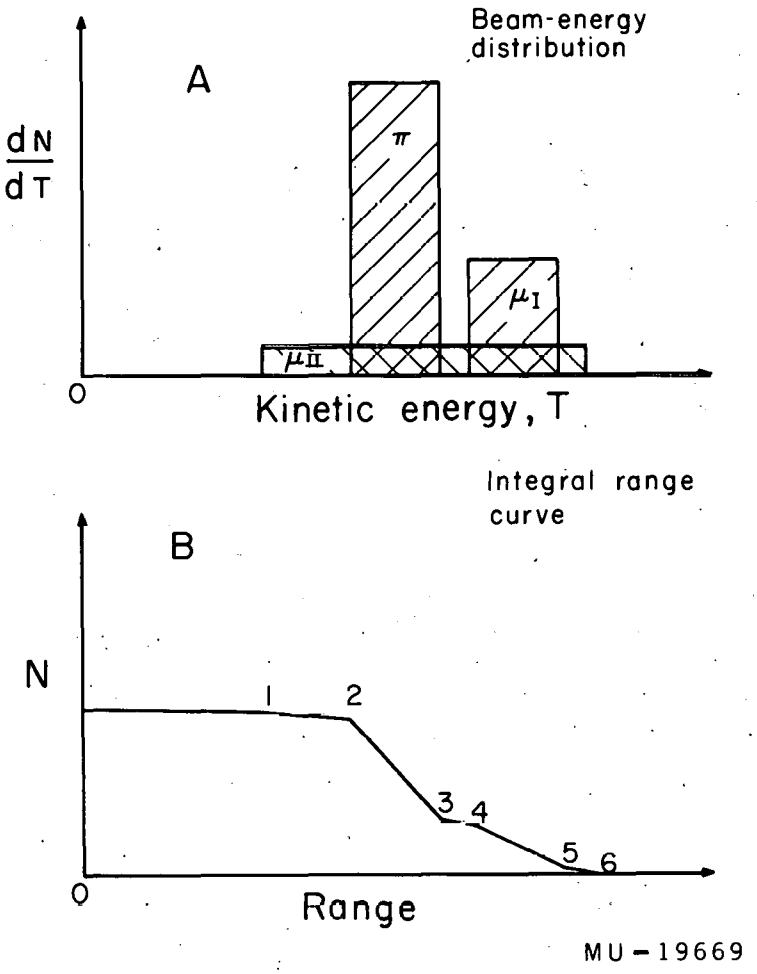

Fig. 14. Idealized pion and muon energy distributions in the beam (A), and the resulting integral range curve expected (B).

thickness. This background arises largely from charge-exchange reactions in the copper. As a result it determines only a rough upper limit on the fraction of electrons present in the original beam when extrapolated to zero copper thickness using measured shower curves.[11] In addition, in all of the range curves obtained in this experiment, by accident points 3 and 4 and points 5 and 6 fall too close together to be distinguishable. This fact was verified by calculating the muon ranges expected from the pion ranges measured.

In practice only three breaks were identified. These are shown in Fig. 3. The breaks are labeled A, B, and C. Break A was identified with idealized break 2, that is the beginning of the pion region. Break B was identified with idealized breaks 3 and 4, the end of the pion region and the beginning of the momentum-analyzed muon region. Break C was identified with idealized breaks 5 and 6, the end of the muons and beginning of the pure electron-shower region. Another point, B', was calculated by extrapolating linearly the electron background back to the range of point B (Fig. 3).

The first information that can be obtained from the range curves is the energy and energy spread of the pions. First, the pion energies corresponding with the pion ranges at points A and B of Fig. 3 are found from range tables.[28] The average of these two energies is the average pion energy. The spread in the pion energy is half the difference between these two energies, after a small correction is made to this difference for range straggling.[15]

The differential range curves (Fig. 3) were used to verify the average energy value for the pion. The position of the maximum in this curve should be about 3 Mev higher than the average obtained from the integral range curve because about that much energy is required for a particle to register in the anticounter used in the differential range-curve measurements. This was found to be true in all instances within inherent errors.

The second piece of information that can be obtained from the range curves is the fraction of muons present in the pion beam. In

order to determine this fraction, first the electron background was extrapolated to get the point, B', (Fig. 3), as discussed above. For the narrow region of ranges involved, a linear extrapolation was considered accurate enough. The difference between the fraction of the incident beam at point B and at point B' is set equal to the fraction of muons in the beam with an energy greater than the energy corresponding to the muon range at point B. Some muons are lost due to multiple coulomb scattering out of the copper absorbers. An estimate of this amount by the method outlined by Perkins[15] showed the loss to be less than 1% in all instances considered here, and thus negligible.

It is necessary to determined the number of muons of lower energy than those found above which have been missed and to correct for them. All of these muons result from pion decays after the analyzing magnet, and as a result it is possible to calculate the number missed. The following is an outline of a simple method to make this calculation with sufficient accuracy.

The method used to find the fraction of muons missed depends upon the fact that for a given-energy pion beam, the decay muons have a rectangular energy distribution in the laboratory system. Furthermore, the muons all go forward inside of a small cone in the laboratory system when the pion energy is in the range of energies encountered in this experiment. In addition, most of the muons are found near the maximum angle of this cone. This latter fact results in a sharp cutoff in the number of muons detected as one considers pion decays farther upstream from the last monitor detector. For the circular detectors used in this experiment, the radius of the detector and the cone angle determine a distance upstream from the detector inside of which all muons are counted and outside of which essentially none are detected. The distance computed in this way can be increased slightly to account for the few muons actually missed. The appropriate factor in this experiment is 1.3, obtained by numerical integration of an actual curve for the number detected as a function of distance from the detector. Because of this threshold characteristic in the muon detection, the muon energy spectrum can still be thought of as being

rectangular with sufficient accuracy. Consequently, the fraction of the muons lost can be found by simple proportion if one knows the maximum and minimum energies of the spectrum expected and the muon energy corresponding to point B in the range curves. These extreme energies and the cone angle in the laboratory system were computed by using the relativistic kinematics program (Appendix B).

The number of muons per pion, p, decaying in the critical length, ℓ, can be determined easily from the known muon lifetime by using the formula

$$p = \ell / \beta\gamma c \tau_{\mu} , \qquad (38)$$

where β and γ are the usual relativistic quantities, and τ_{μ} is the decay mean lifetime for a pion (2.55×10^{-8} sec). Thus the muons missed in the range curve analysis can be determined and added to the muon contamination of the beam.

B. Two-Body Relativistic Kinematics

If a particle of mass M_1 is incident on a particle of mass M which is at rest in the laboratory system of coordinates, the general equation for the interaction can be written as

$$M_1 + M_2 \rightarrow M_3 + M_4 , \tag{39}$$

where particles of masses M_3 and M_4 are produced.

The following quantities are defined:

T_i is the kinetic energy of particle, i

T_{th} is the threshold energy of particle 1.

E is the total relativistic energy for the system

$\bar{\gamma}$ is the value of γ for the center of mass of velocity, $\bar{\beta}$

E_i is the total energy of particle, i

P is the total momentum of the particles

P_i is the momentum of particle, i

θ_i is the angle between the direction of particle 1 and particle i

$d\Omega$ is the differential solid angle of scattering at angle θ.

Barycentric quantities are denoted by an asterisk.

The following general relativistic kinematic formulae hold:

$$T_{th} = \left[(M_3 + M_4)^2 - (M_1 + M_2)^2 \right] / 2M_2 \tag{40}$$

$$E^* = \left[(M_1 + M_2)^2 + 2T_1 M_2 \right]^{1/2} \tag{41}$$

$$\gamma = (T_1 + M_1 + M_2) / E^* \tag{42}$$

$$\overline{\eta} = \overline{\gamma}\,\overline{\beta} = \left[T_1 (T_1 + 2M_1) \right]^{1/2} / E^* \tag{43}$$

$$E_3^* = (E^{*2} + M_3^2 - M_4^2) / 2E^* \tag{44}$$

$$E_4^* = E^* - E_3^* \tag{45}$$

In the following equations, we have i = 3, 4:

$$T_i = E_i^* - M_i \tag{46}$$

$$P^* = (E_i^{*2} - M_i^2)^{1/2} \tag{47}$$

$$P_i = \left[(\overline{\eta} E_i^* + \overline{\gamma} P^* \cos\theta_i^*)^2 + (P^* \sin\theta_i^*)^2 \right]^{1/2} \tag{48}$$

$$T_i = (P_i^2 + M_i^2)^{1/2} - M_i \tag{49}$$

$$\theta_i = \tan^{-1} \left[P^* \sin\theta_i^* / (\overline{\eta} E_i^* + \overline{\gamma} P^* \cos\theta_i^*) \right] \tag{50}$$

$$(d\Omega^*/d\Omega)_i = P_i^3 / \left[P^{*2} (\overline{\gamma} P^* + \overline{\eta} E_i^* \cos\theta_i^*) \right] \tag{51}$$

These formulae were used in the IBM-650 computer program written to obtain tables of scattered pion energies and angles as discussed in Section II, EXPERIMENTAL METHOD. A plot of typical results is shown in Fig. 15, where the energy of the elastically scattered pion and the energy of the most energetic pions produced by reaction 3 are shown as functions of the laboratory angle for an incident pion beam of 370 Mev.

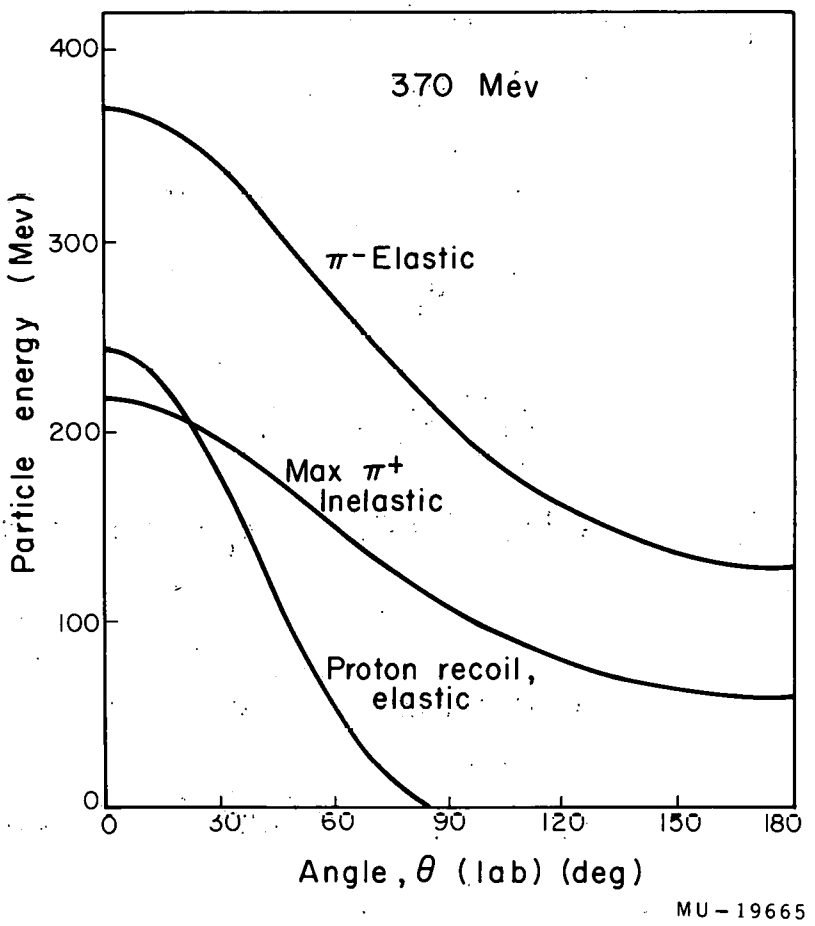

Fig. 15. Relativistic kinematics results in the laboratory system for an incident-pion beam of 370 Mev.

C. The Theory of Least-Squares Fitting

The theory of least-squares fitting employed here is developed in simple form by Cziffra and Moravscik.[29] The following is a summary of the formulae employed.

It is assumed that there are m data points to be fitted of the form $y_i \pm \Delta y_i$ at x_i, where y_i has a standard-deviation error Δy_i, and x_i is exact ($i = 1, 2, \ldots m$). For the purposes of this experiment, a theoretical function to fit these points of the form

$$y = \sum_{j=1}^{n} A_j \phi_j (x) \qquad (52)$$

is chosen, where the ϕ's are arbitrary functions of x only, and the coefficients, A, are to be determined by least-squares fitting.

Least-squares fitting is done by defining the weighted sum, S, of the squares of the residuals, $(y - y_i)$, as

$$S = \sum_{i=1}^{m} (y - y_i)^2 / \Delta y_i^{\,2} \qquad (53)$$

and finding the values of A_j that minimize this sum. This is done in turn by solving the set of n simultaneous equations

$$\partial S / \partial A_k = 0 \,, \qquad (54)$$

for $k = 1, 2, \ldots n$, where the condition $m \geq n$ must hold.

The solution to Eq. (54) can be written in the form

$$A_k = \sum_{j=1}^{n} C_{jk} \sum_{i=1}^{m} y_i \phi_j / (\Delta y_i)^2 \,, \qquad (55)$$

where C_{jk} is the inverse matrix of correlation coefficients for the fit, a symmetrical n - by - n matrix.[30]

The goodness of fit may be tested by applying a χ^2 test. In this instance, where the Δy's are in standard deviations, we have

$$S = \chi^2 , \tag{56}$$

and the degrees of freedom, k, are given by

$$k = m - n .$$

The probability, P, that the value of χ^2 will exceed the value found for a random sample is obtained from tables of χ^2 probabilities for k degrees of freedom,[29] and is a measure of the goodness of fit of the function chosen [Eq. (52)] to the measured points.

In the applications of this experiment, the functions, $\phi(x)$, were either power series,

$$\phi_j(x) = x^{j-1} , \tag{58}$$

or Legendre polynomials,

$$\phi_j(x) = P_{j-1}(x) . \tag{59}$$

Series with increasingly higher values of n were assumed [Eq. (52)], and the smallest value of n with a reasonable χ^2 probability was chosen as the value necessary for an adequate fit.

The value of n found by the χ^2 test was checked by applying the Fisher test for the probability that A_n was zero.[29] For this test, the quantity

$$Q = k(S_{n-1} - S_n) / S_n \tag{60}$$

was calculated, and the probability, F, that it would exceed this value was found in a Fisher (1, k) distribution table.[29]

Having determined the values of A, and C, one can determine the standard deviation error, $\Delta f(x)$, in any function, $f(x)$, from the equation[30]

$$\Delta f(x)^2 = \sum_{i=1}^{n} \sum_{j=1}^{n} C_{ij} \frac{\partial f}{\partial A_i} \frac{\partial f}{\partial A_j} . \qquad (61)$$

In particular, the standard-deviation error in A_k is given from Eq. (61) by the formula

$$\Delta A_k = (C_{kk})^{1/2} . \qquad (62)$$

The standard-deviation error, Δy_c, in computed values of y, y_c, is obtained from Eq. (61) by the formula

$$\Delta y_c^2 = \sum_{i=1}^{n} \sum_{j=1}^{n} C_{ij} \phi_i(x) \phi_j(x) . \qquad (63)$$

The least-squares program written and used computed all of the quantities listed in Eqs. (52) through (63).

D. Finite Target and Telescope Geometry Formulae

More specific formulae for the quantities appearing in Eq. (12) can be given in terms of the coordinate system shown in Fig. 16 for the target and defining counter 3. In these terms, the beam distribution, N(V), is given by

$$N(V) = N(y)\, N(z) , \tag{64}$$

where plots of N(y) and N(z) are shown in Fig. 4. The efficiency, E(V, A), was evaluated from Eq. (6) by first determining the angle, γ, between the line joining the center of the volume and area elements, $\bar{\rho}$, and the x axis by using the equation

$$\cos \gamma = (x_1 - x)/\rho , \tag{65}$$

where

$$\rho = \sqrt{(x_1 - x)^2 + (y_1 - y)^2 + (z_1 - z)^2} . \tag{66}$$

Knowing this angle and the incident beam energy, it was possible to determine the energy of the scattered pion by using the relativistic-kinematics program (Appendix B). Then, the effective thickness of the copper absorber, C_E, was determined from the telescope thickness, C, by using the formula

$$C_E = C/\cos \phi , \tag{67}$$

where the angle, ϕ, between the normal to the counter and $\bar{\rho}$ is given by the formula

$$\cos \phi = [(x_1 - x) \cos \theta + (y_1 - y) \sin \theta] /\rho , \tag{68}$$

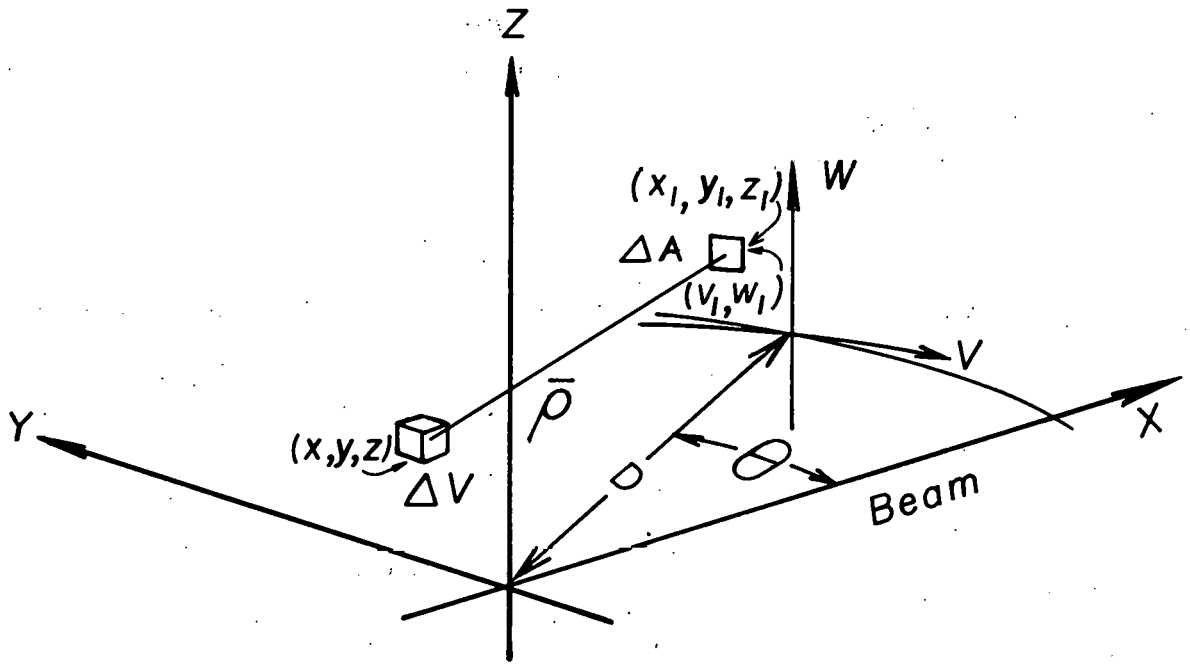

Fig. 16. Idealized geometry used in the corrections for the finite target and counter sizes.

and where ρ is given by Eq. (66). From this energy and effective copper thickness, the efficiency was determined from Eq. (6). The differential-cross-section formula, $F(\gamma)$, was obtained by fitting the laboratory differential cross sections obtained from Eq. (10) with a power series in the cosine of the laboratory angle. This was done by using the least-squares program, the order necessary to give a good fit being determined on the basis of a χ^2 test (Appendix C). The solid angle subtended, $\Delta\Omega(V, A)$, is given by the formula

$$\Delta\Omega(V, A) = \Delta A \cos \phi/\rho^2 , \tag{69}$$

where ρ and $\cos \phi$ are obtained from Eqs. (66) and (68), respectively, and ΔA is the area element.

More specific formulae for x_1, y_1, and z_1 are

$$x_i = D \cos \theta + v_1 \sin \theta , \tag{70}$$

$$y_1 = D \sin \theta - v_1 \cos \theta ,$$

$$z_1 = w_1 ,$$

where v_1 and w_1 are the locations of the center of the area element, ΔA, on the v and w axes centered and lying on the face of counter 3 as shown in Fig. 16. The distance, D, is the distance from the center of the target to the center of counter 3. Values of D used are listed in Table IV.

All of the calculations using Eqs. (64) through (70) above were carried out by the use of the IBM-650 computer. The necessary beam-profile values and relativistic-kinematics results were included in the program in tabular form, all other quantities being determined as discussed above.

REFERENCES

1. H. Bethe and F. de Hoffman, Mesons and Fields II, (Row Peterson and Co., Evanston, Ill., 1955).
2. B. Pontecorvo, Proceedings of the Ninth International Conference on High Energy Physic Kiev, U.S.S.R. (1959).
3. R.R. Crittendon, J.H Scandrett, W.D. Shephard, and W.D. Walker, Phy. Rev. Letters 2, 121 (1959).
4. T.J. Devlin, B.C. Barish, W.N. Hess, V. Perez-Mendez, and J. Solomon, Phys. Rev. Letters 4, 242 (1960).
5. J.C. Brisson, J. Detoef, P. Falk-Vairant, L. van Rossum, G. Valladas, and L.C.L. Yuan, Phys. Rev. Letters 3, 561 (1959).
6. W.D. Walker, J. Davis, and W.D. Shephard, π-Nucleon Phase Shifts in the Energy Range 350 to 600 Mev (preprint), University of Wisconsin, 1950.
7. H.J. Schnitzer and G. Salzman, Phys. Rev. 112, 1802(1958).
8. A. Stanghellini, Nuovo cimento X, 398 (1958).
9. John C. Caris, Charge-Exchange Scattering of Negative Pions by Hydrogen at 230, 260, 290, 317, and 371 Mev, UCRL-9048, March 18, 1960; also J.C. Caris, W. A. Perkins, R.W. Kenney, E.A. Knapp, and V. Perez-Mendez, Bull. Am. Phys. Soc. II 4, 401 (1959).
10. W.G. Cross, Rev. Sci. Instr. 22, 717 (1951).
11. W. Blocker, R.W. Kenney, and W.K.H. Panofsky, Phys. Rev. 79, 419 (1950).
12. J.H. Atkinson and V. Perez-Mendez, Rev. Sci. Instr. 30, 865 (1959).
13. Frank Evans, in Radiation Laboratory Counting Handbook Sec CC3-7, UCRL-3307 Rev., Jan. 1, 1959.
14. D.F. Swift and V. Perez-Mendez, Rev. Sci. Instr. 30, 865 (1959).
15. Walton A. Perkins, III, Positive-Pion Production by Negative Pions (Thesis), UCRL-8778, also, W.A. Perkins, J.C. Caris, R.W. Kenney, E.A. Knapp, and V. Perez-Mendez, Phys. Rev. Letters 3, 56 (1959).

16. D.D. Newhart, V. Perez-Mendez, and W.L. Pope, Liquid-Hydrogen Target UCRL-8857, August 18, 1959.
17. J.C. Caris, L K. Goodwin, R.J. Kenney, V. Perez-Mendez, and W.A. Perkins, (to be published).
18. D.B. Chelton and D.B. Mann, Cryogenic Data Book, UCRL-3421 May 15, 1956.
19. G.F. Chew, and H.P. Noyes, Phys. Rev. 109, 566 (1958).
20. H.P. Noyes, Phys. Rev. 111, 944 (1958).
21. B. Rossi, High Energy Particles, (Prentice Hall, New York, 1952), p. 64.
22. James W. Cronin, Numerical Evaluation of the Pion-Nucleon Forward-Scattering Amplitude, Phys. Rev., to be published (1960).
23. N.S. Mitin and E. L. Grigor'ev, Soviet Physics JETP 5, 378 (1957).
24. G.F. Chew, M.L. Goldberger, F.E. Low, and Y. Nambu, Phys. Rev. 106, 1337 (1957).
25. L.K. Goodwin, R.W. Kenney, and V. Perez-Mendez, Phys. Rev. Letters 3, 522 (1959).
26. J.H. Foote, O. Chamberlain, E.H. Rogers, H.M. Steiner, C. Wiegand, and T. Ypsilantis, Phys. Rev. Letters 4, 30 (1960).
27. S.M. Korenchenko and V.G. Zinov, Soviet Physics JETP 6, 1006 (1958).
28. J.H. Atkinson, Jr., and B.H. Willis, High-Energy Particle Data, UCRL-2426 Rev. II, June, 1957.
29. P. Cziffra and M. J. Moravscik, A Practical Guide to the Method of Least Squares, UCRL-8523, June 5, 1959.
30. W.E. Deming, Statistical Adjustment of Data (John Wiley and Sons, New York, 1948), p. 168.